

1 **Seismic data****A seismic analysis for of** subglacial lake D2 **(Subglacial**
2 **Lake Cheongsuk)** beneath David Glacier, Antarctica

3 Hyeontae Ju^{1,2}, Seung-Goo Kang³, Yeonjin Choi³, Sukjoon Pyun², Min Je Lee³, Hoje Kwak⁴, Kwansoo
4 Kim¹, Yeadong Kim⁵, Jong Ik Lee³

5 ¹Center of Technology Development, Korea Polar Research Institute, Incheon 21990, Korea

6 ²Department of Energy Resource Engineering, Inha University, Incheon 22212, Korea

7 ³Division of Glacier & Earth Sciences, Korea Polar Research Institute, Incheon 21990, Korea

8 ⁴Unit of Antarctic Inland Research, Korea Polar Research Institute, Incheon 21990, Korea

9 ⁵Korea National Committee on Polar Research, Incheon 21990, Korea

10

11 *Correspondence to:* Seung-Goo Kang (ksg9322@kopri.re.kr)

12 **Abstract.** Subglacial lakes beneath Antarctic glaciers are pivotal in advancing our understanding of cryosphere dynamics,
13 basal hydrology, and microbial ecosystems. We investigate the internal structure and physical properties of Subglacial Lake
14 D2 (SLD2), which is located beneath David Glacier in East Antarctica, using seismic data acquired during the 2021/22 austral
15 summer. The dataset underwent a comprehensive processing workflow, including noise attenuation, velocity analysis, and
16 prestack time migration. The migrated seismic sections revealed distinct reverse-~~and normal~~ polarity reflections at the glacier-
17 lake ~~and interface; however, reflections from the lake-bed interfaces, respectively. We compared the synthetic~~
18 ~~seismograms~~sediment interface were ambiguous, leading to interpretational uncertainty about the presence of a sediment layer.
19 To resolve this interpretational uncertainty, two alternative structural models were established: Model 1 (no sediment) and
20 Model 2 (with a sediment layer). Synthetic seismograms generated ~~throughby~~ wave-propagation modeling ~~on the basis of our~~
21 ~~structural interpretation of the migrated sections with the~~ were compared with field data to validate the subglacial lake structure
22 ~~inferred from the seismic data. This~~ The results confirmed ~~that~~ the water column thickness ranged from to be approximately
23 ~~53 to 82 m (Model 1) or approximately 10 m (Model 2), and delineated the broader structure of possible structural scenarios~~
24 ~~for~~ the subglacial lake were presented. Additionally, discontinuous reflections detected in seismic sections transverse to the
25 ice flow were interpreted as scour-like feature surfaces formed by ice movement. ~~A comparison with airborne ice penetrating~~
26 ~~radar (IPR) data acquired in 2018 further supported the consistency of the ice thickness estimates. Notably, a steeply dipping~~
27 ~~bedrock boundary identified along profile 21YY provided a more precise definition of the lateral extent of SLD2 than was~~
28 ~~possible when IPR data alone were used. This study identified the basal structure beneath the subglacial lake, which had been~~
29 ~~challenging to identify with conventional radar surveys, through seismic surveying. In addition, ambiguous signals in the field~~
30 ~~seismic data were mitigated via quantitative comparison with synthetic data, thereby facilitating interpretation of the~~
31 ~~underlying structure.~~ Collectively, these findings enhance our understanding of subglacial lake environments and inform the
32 selection of future drilling sites for in situ sampling.

33 **1 Introduction**

34 Subglacial lakes beneath the Antarctic ice sheet are typically overlain by glaciers several kilometers thick and have remained
35 isolated from direct atmospheric and solar influences for millions of years, creating extreme environments characterized by
36 low temperatures (Thoma et al., 2010) and high pressures (Tulaczyk et al., 2014). With increasing scientific interest, subglacial
37 lakes have become a focal point for studies related to the Antarctic paleoclimate, as inferred from lake sediments, as well as
38 investigations into microbial life in polar ecosystems (Bell et al., 2007, 2011; Bentley et al., 2009; Christner et al., 2014;
39 Engelhardt et al., 1990; Priscu and Christner, 2003; Rose, 1979; Wingham et al., 2006). Subglacial lakes in Antarctica are
40 generally categorized as either stable or active. Approximately 80% of subglacial lakes in Antarctica are classified as stable
41 subglacial lakes. These closed systems do not exhibit significant surface elevation changes and where are characterized by
42 long-term balance between recharge and discharge, although the extent of subglacial water remains largely isolated, with
43 minimal exchange due to slow and stable recharge and discharge cycles remains uncertain in the absence of direct observations.

44 The remaining 20% are classified as active subglacial lakes, which exhibit surface elevation changes due to episodic water
45 drainage and refilling events (Livingstone et al., 2022). Such active lakes can reduce basal friction as they expand, thereby
46 facilitating glacier flow and, in some cases, accelerating calving processes, ultimately influencing glacier dynamics (Bell et
47 al., 2007; Stearns et al., 2008; Winsborrow et al., 2010). Characterizing subglacial lakes is essential for understanding
48 cryospheric processes, reconstructing past climate conditions, and assessing the potential for life in isolated, extreme
49 environments.

50 The sampling of subglacial lake water, sediments, and microbial communities is critical to address these scientific objectives.
51 However, successful sampling requires careful selection and characterization of the drilling site. Airborne ice-penetrating radar
52 (IPR) surveys are commonly employed at regional scales to detect potential subglacial lakes suitable for drilling (Christianson
53 et al., 2012; Lindzey et al., 2020; Yan et al., 2022). However, due to signal attenuation in water, IPR surveys are limited in
54 resolving the internal structure of subglacial lakes. To overcome this limitation, seismic surveys have been conducted at
55 potential subglacial lake candidates identified from IPR surveys. During such surveys, P-waves propagate through the water
56 column and are partially reflected at the lake–bed interface because of contrasts in acoustic impedance. Analyzing these
57 reflected waves enables detailed delineation of the water column and underlying substrate, thereby informing optimal drilling
58 locations (Brisbourne et al., 2023; Filina et al., 2008; Horgan et al., 2012; Woodward et al., 2010).

59 As such, numerous studies have utilized seismic surveys to investigate the characteristics of subglacial lakes, including
60 Subglacial Lake Ellsworth, Subglacial Lake Whillans, and Subglacial Lake CECs. Subglacial Lake Ellsworth, located beneath
61 2,930–3,280 m of glacial ice in West Antarctica, was the subject of a seismic survey during the austral summer of 2007–08.
62 This survey revealed spatially variable ice thickness and a lake water column ranging from 52 to 156 m, which guided the
63 identification of an optimal drilling location (Smith et al., 2018; Woodward et al., 2010). Subglacial Lake Whillans lies beneath
64 approximately 800 m of ice. Seismic observations conducted during the 2010/11 field season revealed water columns
65 extending over a 5 km segment of the survey profile, with a maximum thickness of less than 8 m. The glacier bed was

66 predominantly composed of soft sediments, and localized zones with shallow water columns (< 2 m) were also identified
67 (Horgan et al., 2012). Subsequent drilling in the summer of 2012/13 confirmed the presence of microbial life in both the water
68 and sediment samples (Christner et al., 2014). Subglacial Lake CECs (SLCECs), located beneath 2653 m of ice at the Rutherford–
69 Institute–Minnesota Divide in West Antarctica, were investigated through seismic surveys conducted in the 2016/17 and
70 2021/22 seasons. These surveys revealed a maximum water column thickness of 301.3 ± 1.5 m and clastic sediments up to 15
71 m thick covering the lakebed. While the lake center was relatively flat, significant topographic variability was observed near
72 the lake margins (Brisbourne et al., 2023).

73 We have initiated subglacial lake research beneath David Glacier, the closest major glacier to Jang Bogo Station in East
74 Antarctica. Satellite altimetry has identified six subglacial lakes in this region (Smith et al., 2009; Wright and Siegert, 2012).
75 During the 2016/17 austral summer, an airborne IPR survey was conducted over the region encompassing Subglacial Lake D1
76 (SLD1) and Subglacial Lake D2 (SLD2) (Lindzey et al., 2020). A subsequent high-resolution IPR survey was carried out
77 during the 2018/19 field season, focusing solely on SLD2 (Ju et al., 2025). ~~The combined results of the two surveys revealed
78 moderately enhanced radar bed echoes relative to the surrounding area, specularity values (>0.4), a depressed basal elevation
79 (< 350 m), and a low hydraulic gradient (< 0.84°), collectively indicating high potential for the presence of subglacial water
80 beneath SLD2. Building upon these observations, also referred to as “Subglacial Lake Cheongsuk”~~ (Ju et al., 2025). Ju et al.
81 (2025) subdivided the previously identified single subglacial water body at SLD2, as detected by ICESat altimetry, into three
82 smaller subglacial lakes: SLD2-A, SLD2-B, and SLD2-C. Among these, SLD2-A represents the largest areal extent, and
83 targeted seismic surveys were conducted over this area to obtain high-resolution information on the lake depth and basal
84 structure. In the 2019/20 season, an initial seismic campaign identified the glacier thickness and suggested the presence of the
85 lake; however, the data quality was compromised by surface crevasse noise and a lack of adequate fold coverage, limiting
86 detailed interpretation. A refined seismic survey with 8-fold coverage was conducted during the 2021/22 season to address
87 these issues. ~~Furthermore, the sound source was positioned further from the crevasse (end-shot), delaying the arrival of
88 crevasse-generated noise and preventing it from obscuring key reflections.~~

89 In this study, we present a detailed analysis of the physical and structural properties of SLD2-A using seismic data acquired
90 during the 2021/22 campaign. We first describe the seismic data processing workflow, including noise attenuation, amplitude
91 correction, and prestack time migration. ~~The final results reveal seismic reflections corresponding to the glacier–lake and lake–
92 bed interfaces. The seismic interpretation is subsequently validated through a comparison with synthetic seismograms, and a
93 quantitative analysis is performed to determine the key structural characteristics of SLD2-A, including the ice thickness, water
94 column thickness, and basal structure of the lake. Some areas of the processed field seismic data are challenging to interpret
95 due to a lack of subsurface information, overlap with ghost signals, and signal attenuation. In the case of the SLD2 region, the
96 absence of borehole data introduces inherent uncertainty into the subglacial lake structure derived from the Prestack Time
97 Migration (PSTM) section. In particular, reflections associated with the sediment layer are challenging to interpret because
98 they have weak amplitudes and overlap with ghost components. To compensate for these limitations, a subsurface structural
99 model was constructed, and model-based synthetic seismograms were compared and analyzed against field observations. As~~

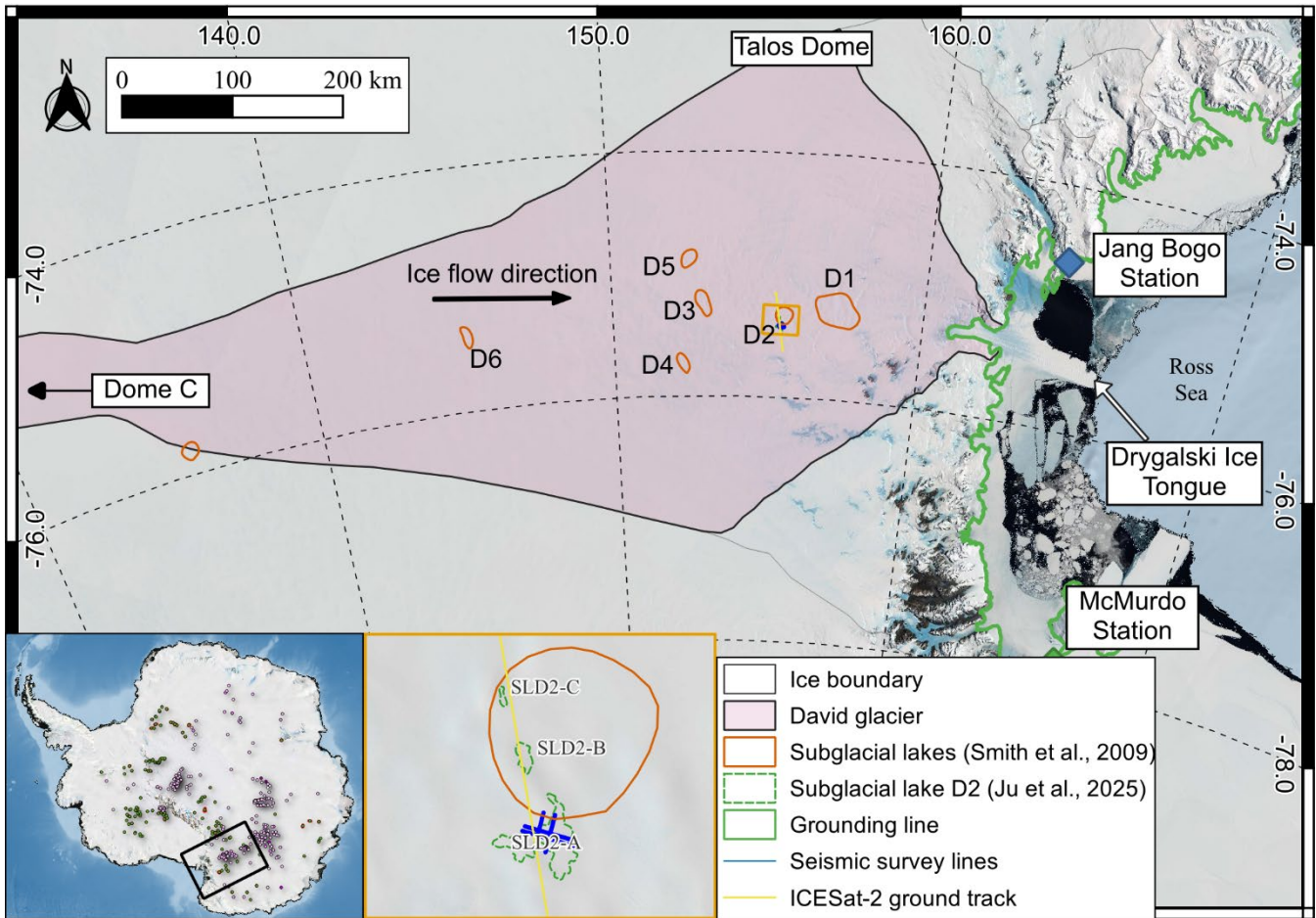
100 a result, the substructure of SLD2-A is quantitatively presented as two possible scenarios: Glacier–Lake–Bedrock (model 1)
101 or Glacier–Lake–Sediment–Bedrock (model 2).

102 **2 Subglacial Lake D2 Beneath David Glacier in Antarctica**

103 **2.1 David Glacier**

104 David Glacier, located in Victoria Land, East Antarctica, originates from the Dome C and Talos Dome regions and flows
105 seaward through the Drygalski Ice Tongue (Fig. 1). The mass balance of glaciers from 1979 to 2008 has been estimated at 7.5
106 ± 0.4 Gt yr $^{-1}$ (Rignot et al., 2019), while the mean ice discharge over the more extended period from 1979 to 2017 was reported
107 to be approximately 9.7 Gt yr $^{-1}$ (Frezzotti et al., 2000; Rignot et al., 2019). According to Smith et al. (2020), satellite altimetry
108 observations from ICESat-1 and ICESat-2 (2003–2019) indicate that the grounded portion of David Glacier experienced a mass
109 gain of 3 ± 2 Gt yr $^{-1}$, whereas the adjacent ice shelves exhibited a mass loss of -1.6 ± 1 Gt yr $^{-1}$. Although the overall mass
110 balance of David Glacier currently appears stable, it remains uncertain how long this stability can be maintained. several active
111 subglacial lakes observed by satellites have the potential to influence glacier dynamics (Ju et al., 2025; Kim et al., 2025).

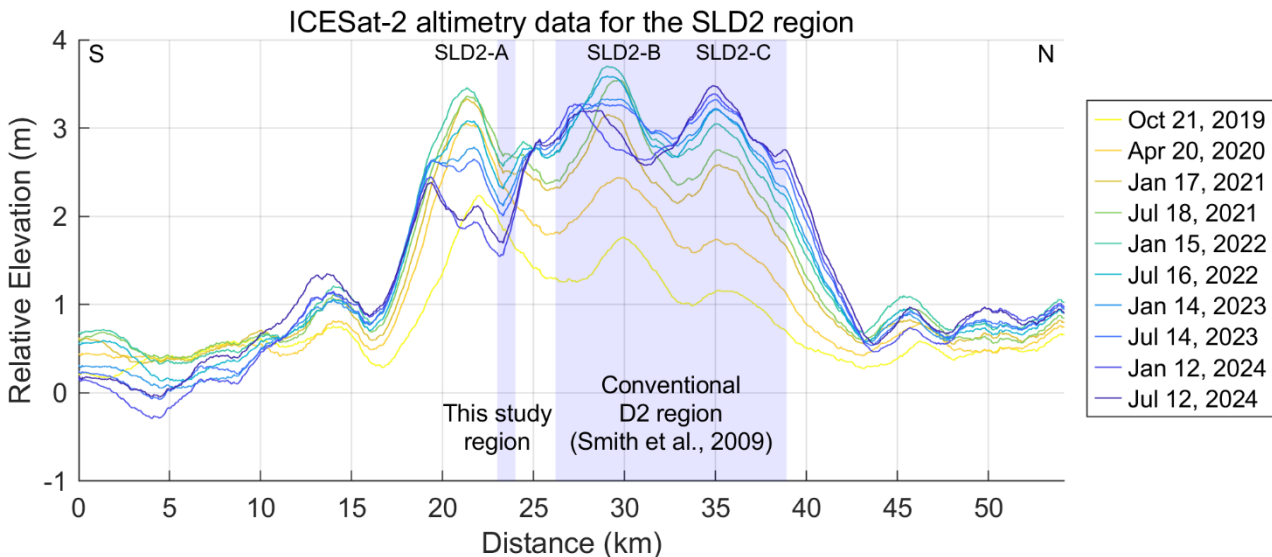
112



113
114 **Figure 1: Locations of subglacial lakes D1–D6 in the David Glacier region, Victoria Land, Antarctica (EPSG: 4326–WGS84).**
115

116 2.2 Subglacial Lake D2

117 Among the six subglacial lakes (D1–D6) identified beneath David Glacier via satellite altimetry (Smith et al., 2009; Wright
118 and Siegert, 2012), SLD2 was observed to have experienced a drainage event between 2003 and 2008 on the basis of ICESat
119 altimetry data (Smith et al., 2009). Since the drainage event, a continuous increase in surface elevation over SLD2 has been
120 observed, indicating water refilling, as detected from CryoSat-2 altimetry data (2013–2017) (Siegfried and Fricker, 2018) and,
121 more recently, from ICESat-2 observations (2019–2024) (Fig. 2). Figure 2 shows elevation changes relative to April 2019,
122 indicating surface uplift through January 2022. After this period, the surface elevation remained stable in the region originally
123 delineated as SLD2 by Smith et al. (2009), whereas a decreasing elevation trend was observed in the SLD2-A region (Ju et al.,
124 2025). These patterns of elevation change strongly suggest that SLD2 is an active subglacial lake, with cyclic drainage and
125 refilling likely contributing to the presence of subglacial sediments. (Siegfried et al., 2023).



127

128 **Figure 2: Glacier surface elevation changes derived from ICESat-2 altimetry between 22 April 2019 and 12 July 2024. The X-axis**
 129 **corresponds to the 22 April 2019 dataset, and all subsequent elevation changes are referenced to this date. The light blue shaded**
 130 **region indicates the spatial overlap between the conventional SLD2 region identified by Smith et al. (2009) and our study region.**

131

132 To better constrain the lake's extent and basal conditions of SLD2, we used airborne IPR survey data from collected during the
133 2016/17 (Lindzey et al., 2020) and 2018/19 (Ju et al., 2025) field campaigns indicate. These surveys show that the glacier
134 surface elevations in the SLD2 region range from approximately 1820 to 1940 m, with. The corresponding ice thicknesses
135 vary between 1685 and 2293 m. Furthermore, the observations of moderately enhanced radar bed echoes relative to
136 the surrounding area, elevated specularity values (>0.4), depressed basal elevations (≤-350 m), the presence of a Bain basin-
137 like topography, a lower hydraulic head than the surroundings, and low hydraulic gradients ($\leq 0.84^\circ$) collectively suggest a
138 high potential for the presence of subglacial water beneath SLD2. (Ju et al., 2025; Lindzey et al., 2020).

139 3 Method

140 3.1 Seismic survey

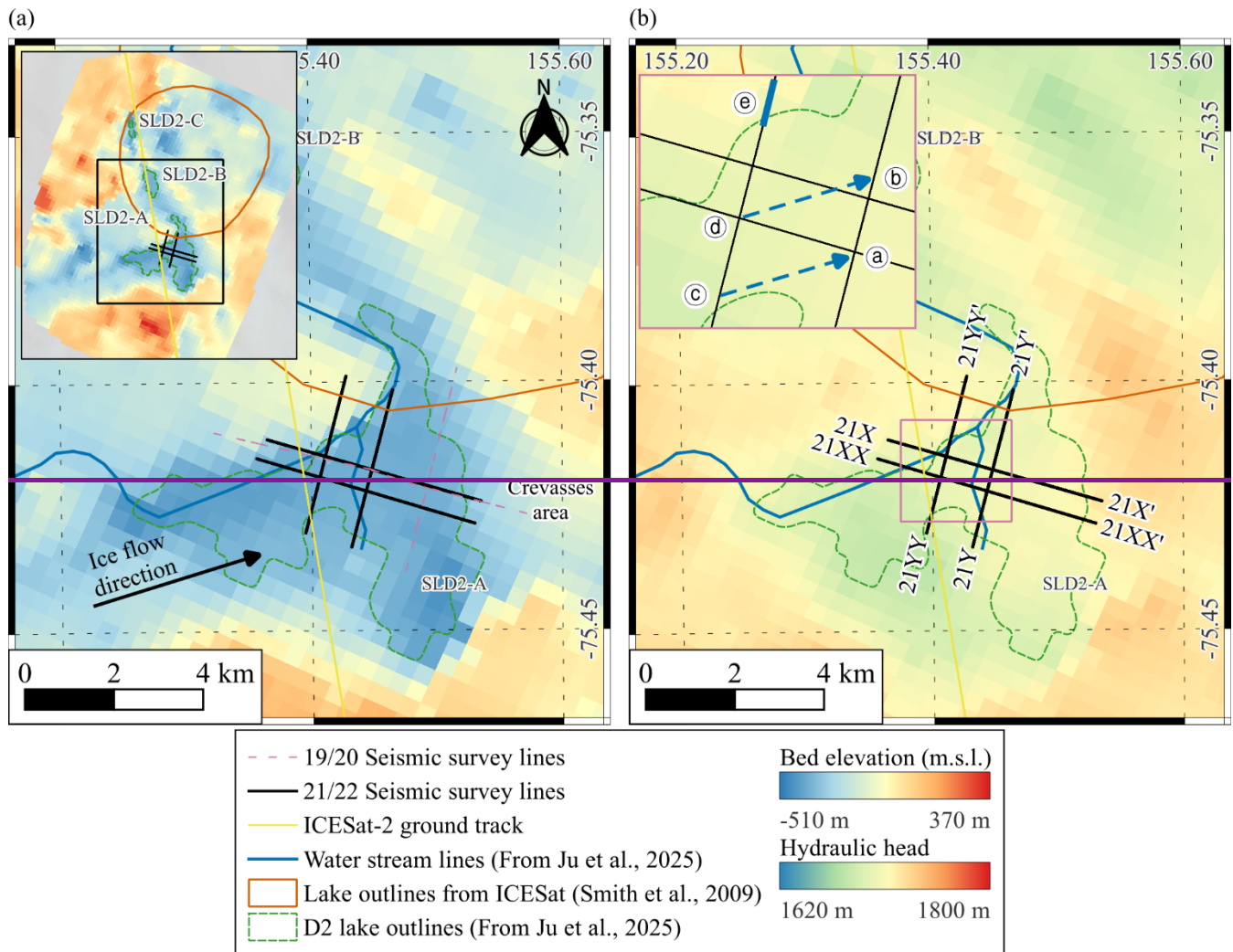
141 As previously noted, the internal structure and water column of subglacial lakes cannot be fully resolved using IPR alone
142 because of signal attenuation in water. Accordingly, a seismic survey was conducted within the candidate SLD2-A region
143 identified from IPR data to investigate the structure of the subglacial lake more precisely.

144 During the 2019/20 austral summer, a preliminary seismic survey was conducted over the SLD2-A region to evaluate the
145 potential presence of a subglacial lake and to obtain initial information on its structural characteristics. Owing to limited field
146 time and equipment constraints, the fold of coverage for all survey lines was restricted to 1, and all shot points ~~were~~ happened

147 to be aligned near surface crevasses. Consequently, the acquired seismic data were significantly contaminated/degraded by
148 strong linear coherent noise associated with generated by crevasses, which severely degraded compromising the signal quality
149 of key reflectors, particularly reflections from those at the subglacial lake–bedrock interface. In addition Furthermore,
150 explosives are/were deployed within shallow boreholes (< 20 m depth), and owing due to the absence of proper backfilling
151 and the rapid timing of detonation, poor coupling between the explosives and the borehole walls further reduced/reduced energy
152 transmission efficiency, resulting in overall low-quality reflection signals (Ju et al., 2024). As a result, due to Combined with
153 the limitations of single-fold acquisition, stacking was not feasible, resulting in the dataset exhibited a low signal-to-noise ratio
154 (SNR) and the presence of dominant coherent noise, rendering the seismic dataset was unsuitable for quantitative structural
155 interpretation. Nevertheless, the preliminary survey qualitatively confirmed the glacier thickness beneath SLD2-A and
156 suggested the presence of subglacial water, providing critical baseline information that guided the methodology and survey
157 design of the subsequent detailed seismic campaign conducted during the 2021/22 season.

158 For the refined survey, seismic acquisition lines were planned using bed topography derived from the IPR and surface elevation
159 data from satellite altimetry. A total of four seismic lines were acquired and designated 21X, 21Y, 21XX, and 21YY (Fig. 3).
160 Lines 21X and 21XX, oriented approximately 52.60° relative to the ice flow direction, are situated at an average surface
161 elevation of 1894 ± 13 m. Lines 21Y and 21YY, oriented approximately -30° in the ice flow direction, lie at an average
162 elevation of 1887 ± 16 m. All lines traverse regions of minimal topographic relief, with average surface slopes of approximately
163 0.5°, indicating a relatively flat and stable glacier surface. The lengths of the 21X/21XX and 21Y/21YY lines are
164 approximately 5 km and 3.5 km, respectively. Seismic acquisition for lines 21X and 21Y was conducted using 8-fold coverage
165 to increase the resolution, whereas lines 21XX and 21YY were acquired with 4-fold coverage due to time constraints during
166 the survey. The additional acquisition parameters are summarized in Table 1.

167



Survey Parameters	Survey lines			
	21X line	21Y line	21XX line	21YY line
Line length (km)	5	3.5	5	3.5
Fold	8	8	4	4
Shot interval (m)	90	90	180	180
Number of shots	56	40	28	20
<u>Shot positioning</u>	<u>Use both off-end and center shots</u>			
Receiver channels	96			
Receiver interval (m)	15			

Near offset (m)

0

Far offset (m)

1425

Recording time (s)

4

Record peak frequency (kHz)

1

Record sampling rate (ms)

0.25

Survey time (days)

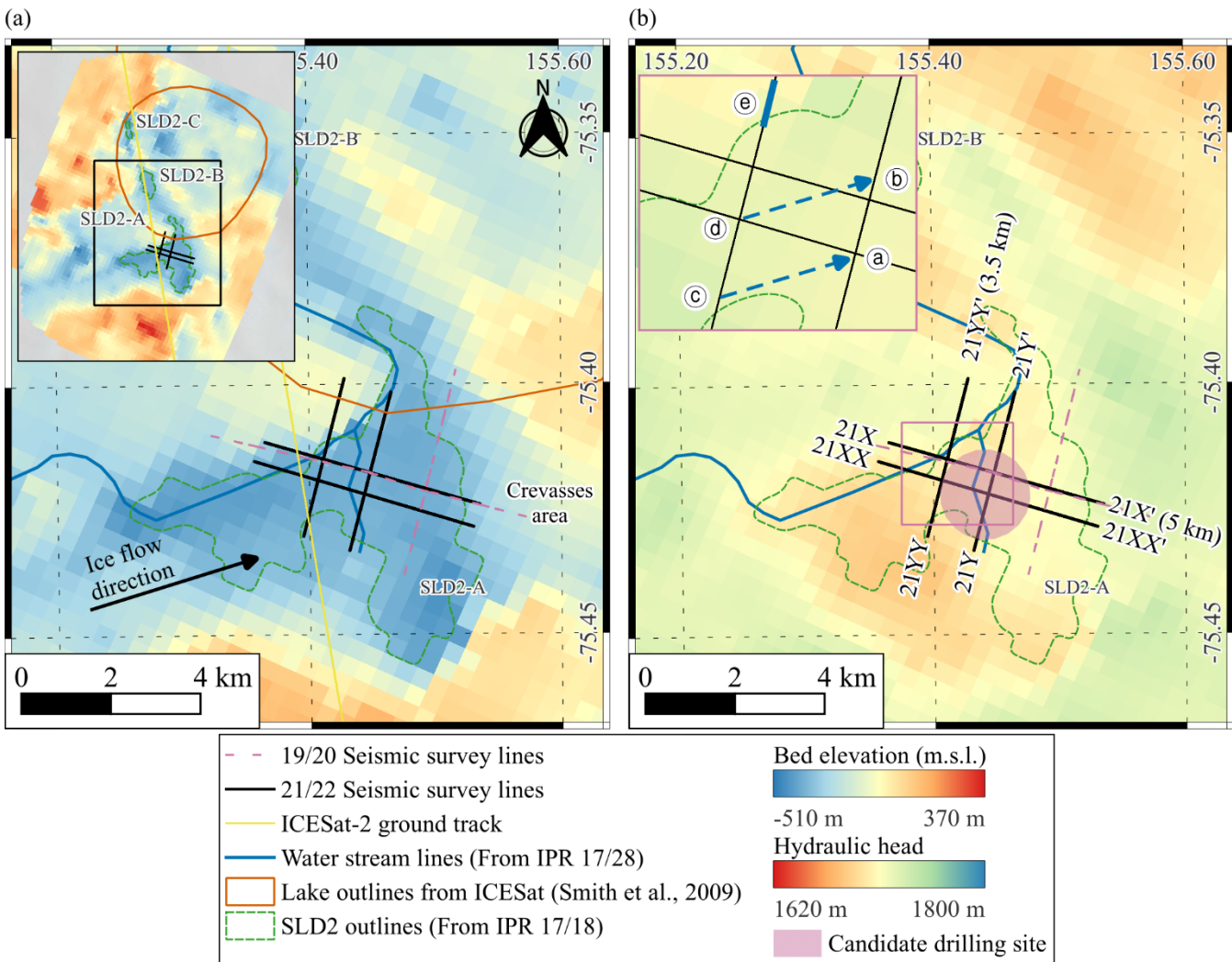
34

Survey crew size

3

Hot water drilling (3), Seismic (6)

173



174

175 **Figure 3: 21/22 seismic survey layout (black lines) overlaid on (a) bed elevation and (b) hydraulic head data from IPR results (Ju et al., 2025).**

176

177

178 Before the seismic survey, a ground-penetrating radar (GPR) survey was used to identify the firn transition zone at depths of
179 approximately 20–22 m. To enhance seismic signal transmission, 1.6 kg of pentaerythritol tetranitrate (PETN) explosives were

180 emplaced at depths of 25–30 m using hot water drilling techniques. A total of 144 shots were deployed across the four survey
181 lines. [Detailed shot positioning information is provided in the supplementary information S1](#). Given the snow-covered glacier
182 surface, Georods were used instead of conventional spike-type geophones to increase signal detection efficiency (Voigt et al.,
183 2013). Each Georod houses four geophone elements in a 0.6 m-long cylindrical array, producing a single output by summing
184 the inputs from all the elements. Compared with traditional geophones, this configuration improves coupling and detection
185 performance in snow-dominated environments (JuVoigt et al., [20242013](#)). Figure 4 presents shot gather #27 from line 21X
186 and shot gather #7 from line 21Y. In these shot gathers, the velocity of the direct wave is estimated to be approximately
187 1800 m/s, and the refracted wave velocity [in firn-ice transition](#) is approximately 3800 m/s. First-arrival analysis of the direct
188 wave indicates a normal polarity, confirming the source waveform polarity. A prominent negative polarity reflection is
189 observed at a two-way travel time (TWT) of approximately 1.2 s, interpreted as the glacier–lake interface-[\(1\)](#); [See Table 2](#)
190 [for symbols definitions](#)). Approximately 25–30 ms later, a ghost reflection [\(2\)](#) with normal polarity appears. A subsequent
191 reflection at approximately 1.3 s TWT, showing normal polarity, is attributed to the [lake](#)–bed interface;[\(5\)](#), followed by its
192 negative polarity ghost reflection [\(6\)](#) 25–30 ms later. In [some](#) shot [gather](#)[gathers](#), reflection signal [\(3\)](#) and its corresponding
193 [ghost signal](#) [\(5\)](#) [are observed](#). Notably, while signal [\(3\)](#) [generally appears with normal polarity in most records](#), it appears
194 [with reverse polarity in a few cases](#), such as Shot #27, [noise originating](#) on line 21X. The survey was designed to place the
195 [seismic source at a distance](#) from crevasses [becomes apparent from approximately 2 s TWT](#). [As the distance to](#), [ensuring that](#)
196 [crevasse-related noise would be recorded after](#) the [crevasses decreases](#), [main reflections](#) (1.1–1.3 s), thereby minimizing its
197 [impact](#) (Figure 4a). While most data exhibit crevasse noise occurring after the main reflections, a reduction in the source–
198 [crevasse distance causes](#) this noise [to](#) [increasingly overlap](#)[overlap](#) with the primary [reflection](#) arrivals, [thereby](#) complicating
199 [the](#) interpretation.

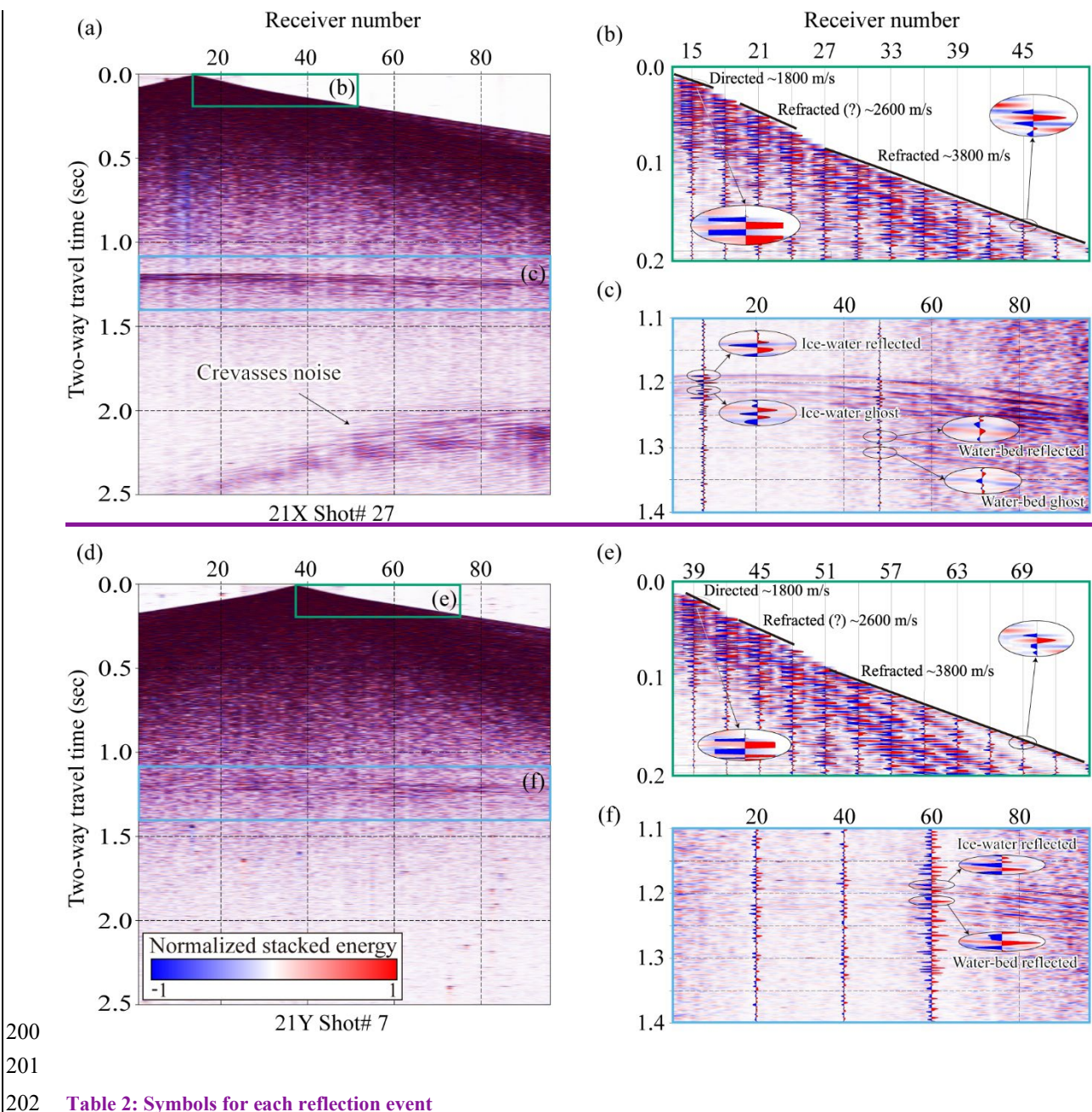
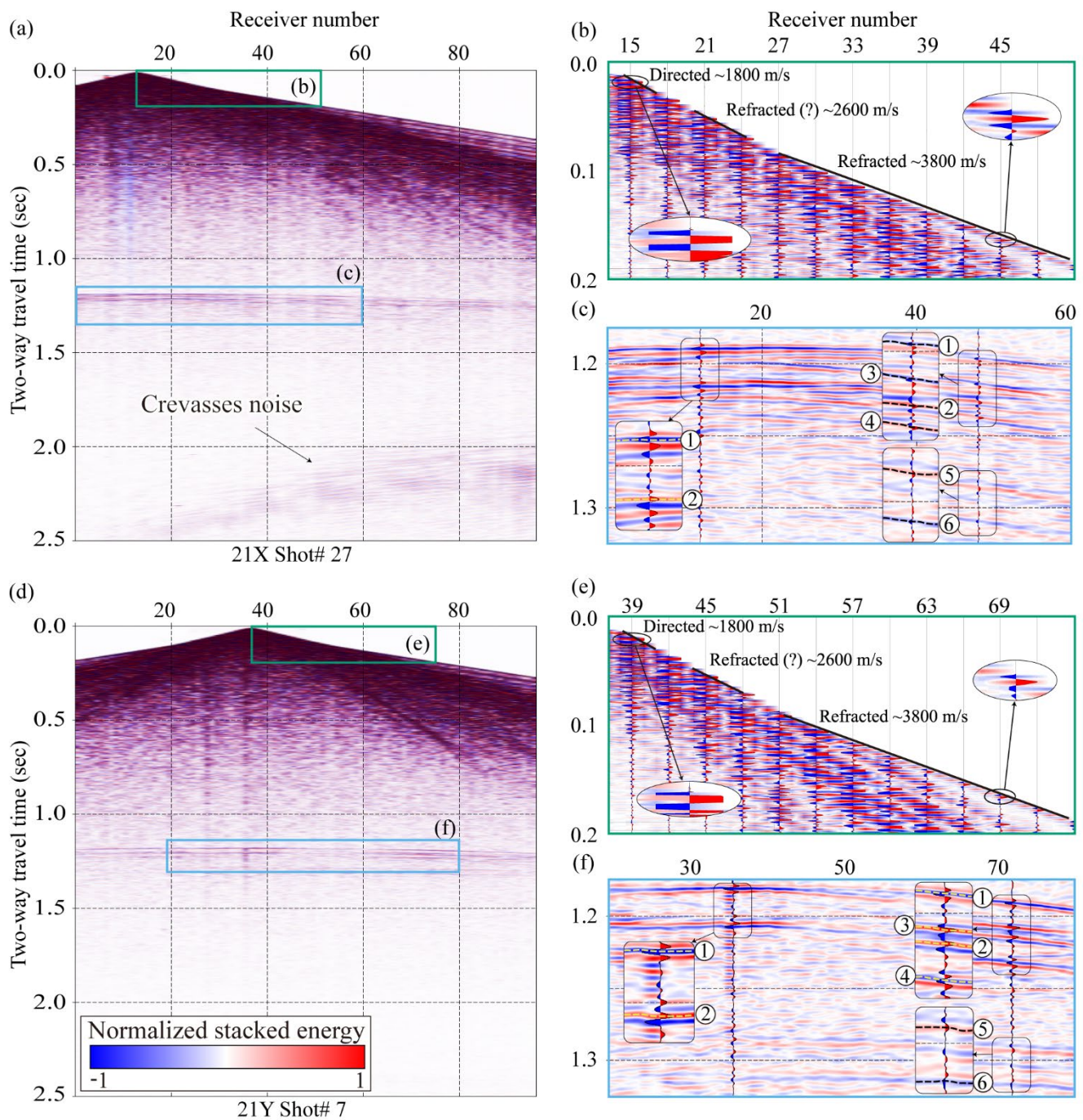


Table 2: Symbols for each reflection event

Interface symbols	Model 1	Model 2
①	<u>Ice-water</u>	<u>Ice-water</u>
②	<u>Ice-water ghost</u>	<u>Ice-water ghost</u>
③	-	<u>Water-sediment</u>
④	-	<u>Water-sediment ghost</u>
⑤	<u>Water-bed</u>	<u>Sediment-bed</u>

<u>⑥</u>	Water-bed ghost	Sediment-bed ghost
<u>⑦</u>	Ice-bed	Ice-sediment
<u>⑧</u>	Ice-bed ghost	Ice-sediment ghost

203



204

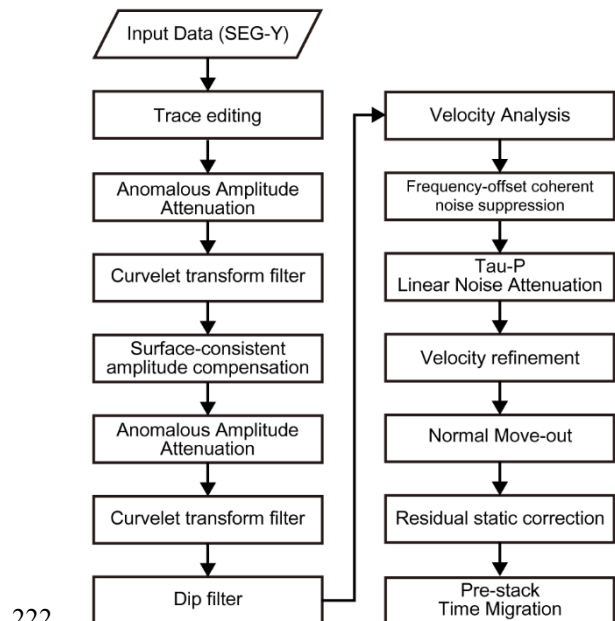
205 **Figure 4: Raw shot records from seismic lines 21X (a) and 21Y (d). Panels (b) and (e) are zoomed-in views of the early arrival window**
 206 **(0.0–0.2 s)** from panels (a) and (d), respectively, used to calculate the apparent velocities of the direct and refracted waves. These
 207 **panels highlight that the first arrivals of both the direct wave (clipped for display) and the refracted wave exhibit positive polarity.**
 208 **The direct wave, propagating through the upper firn layer (0–25 m depth), shows an apparent velocity of approximately 1800 m/s,**
 209 **while the refracted wave ~~traveling through glacier ice in firn-ice transition~~ has an apparent velocity of approximately 3800 m/s.**
 210 **Panels (c) and (f) are zoomed-in views of the deeper arrivals (1.1–1.4 s) from panels (a) and (d), respectively. Reflections from the**
 211 **ice–water (①) interface exhibit negative polarity, whereas those from the water/sediment–bed (⑤) interface display positive polarity.**

212

213 3.2 Seismic data processing

214 Although seismic data acquired from glaciers share processing similarities with those of land-based surveys, glaciological
 215 factors, such as surface cracks, crevasses, and strong winds, introduce substantial noise that can degrade data quality (Johansen
 216 et al., 2011; Zechmann et al., 2018). Among these factors, linear noise generated by crevasses is particularly detrimental, often
 217 obscuring key reflections (Dow et al., 2013). Hence, the glacier seismic data underwent multiple data processing sequences
 218 focused on linear noise removal (Fig. 5). Acquisition geometry was added to the data using the raw data and geometry
 219 information. Multiple data processing and noise removal processes were then carried out to increase the signal-to-noise ratio
 220 (SNR).

221



222
 223 **Figure 5: Schematic of the seismic data processing workflow based on the Omega geophysical data processing platform (SLB),**
 224 **including noise attenuation, amplitude correction, velocity analysis, and prestack time migration.**

225

226 The initial processing involved anomalous amplitude attenuation (AAA), implemented via a spatial median filter. This step
227 targets outlier amplitudes within a defined frequency band, attenuating anomalous signals through interpolation across
228 neighboring traces. A curvelet transform-based filter was subsequently applied to remove coherent noise. Curvelet
229 decomposition enables the separation of signals on the basis of dip angle and scale, allowing for the selective removal of
230 ground roll and other coherent noise components that differ in dip from true reflections (Oliveira et al., 2012). In this study,
231 linear coherent noise at later arrival times (>2.0 s) was effectively removed using this method.

232 Surface-consistent amplitude compensation (SCAR) and surface-consistent deconvolution were employed to normalize the
233 amplitude variability across shot gathers. These steps were followed by a second round of AAA and curvelet filtering to
234 suppress artifacts introduced during the compensation and deconvolution stages. Dip filtering was also applied to eliminate
235 spurious hyperbolic arrivals, which were manually identified and removed.

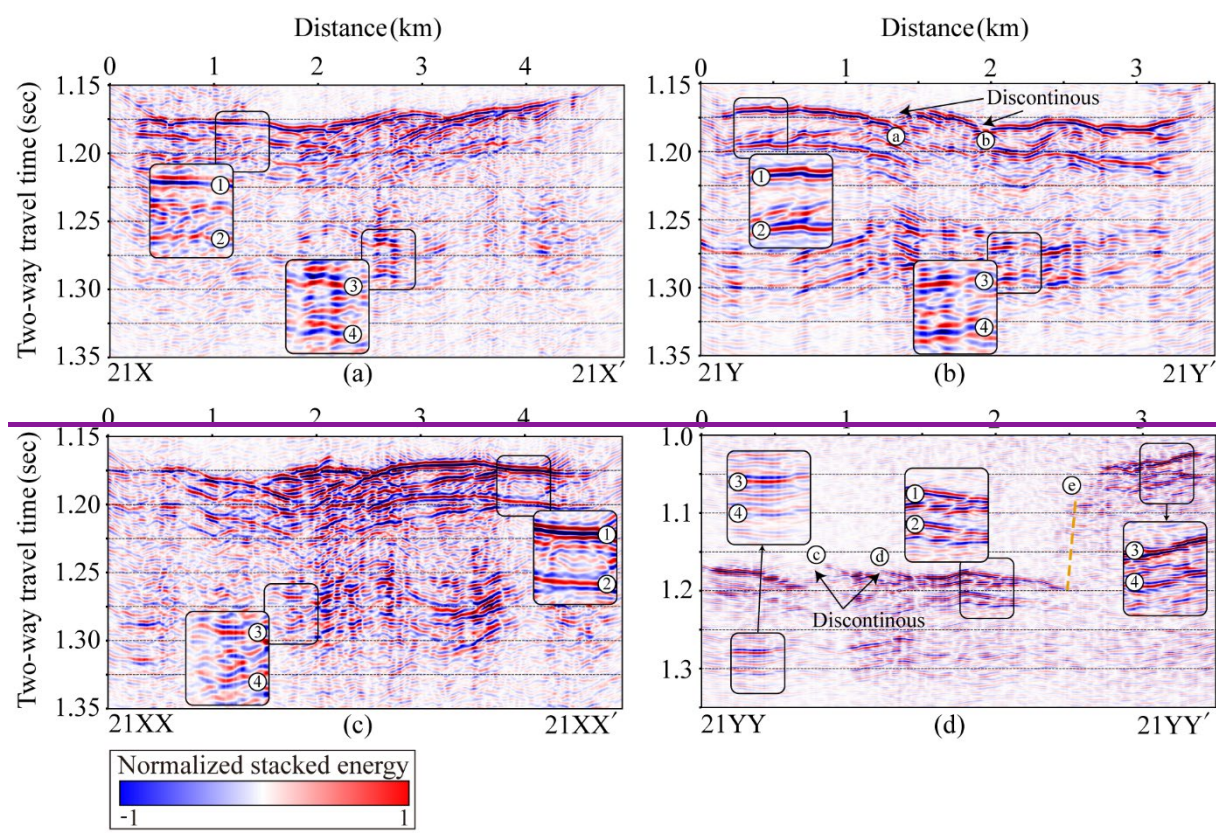
236 Velocity analysis was conducted at intervals of 40 common midpoints to construct a migration velocity model. Frequency–
237 offset coherent noise suppression (FXCNS) was used to attenuate linear-related noise, followed by Tau-p linear noise
238 attenuation (LNA), effectively reducing the noise associated with crevasse scattering. The final processing steps included
239 velocity model refinement, normal move-out (NMO) correction, and prestack time migration (PSTM). The specific parameters
240 employed for data processing, as well as the intermediate outcomes at each processing stage, are provided in the supplementary
241 information ([S1](#);[S2](#)).

242 To increase imaging accuracy, a residual static correction was applied before migration using glacier surface elevation data.
243 The final migrated seismic section was produced using Kirchhoff PSTM. The migrated data have a center frequency of
244 approximately 180 Hz. Assuming seismic wave velocities between 1395 m/s and 3800 m/s, the corresponding vertical
245 resolutions, which are calculated using the quarter-wavelength criterion, range from approximately 2.01 m to 5.27 m. [This](#)
246 [resolution is adequate for imaging SLD2](#)[The data can image both the top and bottom of a water column approximately 2 m](#)
247 [thick or thicker.](#)

248 4 Seismic data processing results

249 Figure 6 presents the PSTM results for the four seismic survey lines. On line 21X (Fig. 6a), a strong, laterally continuous
250 reflection with reverse polarity is observed at 0.3–4.8 km along the profile, and the two-way travel time (TWT) is
251 approximately 1.15–1.18 s. This reflection is interpreted as the glacier–lake interface (①). Approximately 25–30 ms below
252 this horizon, a normal-polarity reflection (②) appears, likely representing a ghost signal associated with the primary glacier–
253 lake reflection. [Between reflections ① and ②, a weak normal polarity reflection \(③\), presumed to represent an interface, is](#)
254 [observed. However, in some shot gathers, signal ③ appears with reverse polarity \(Figure 4c\), leading to partial cancellation](#)
255 [and ambiguity in layer interpretation. Approximately 25 ms later, an opposite polarity ghost reflection \(④\) follows.](#) A deeper
256 normal-polarity reflection is observed within 1.9–3.1 km at TWTs of 1.25–1.27 s (③⑤), which is interpreted as the lake

257 bed interface. This is followed by a reverse-polarity reflection 25–30 ms later (4–6), which is presumed to be the
258 corresponding ghost of the lake-bed interface.
259



260

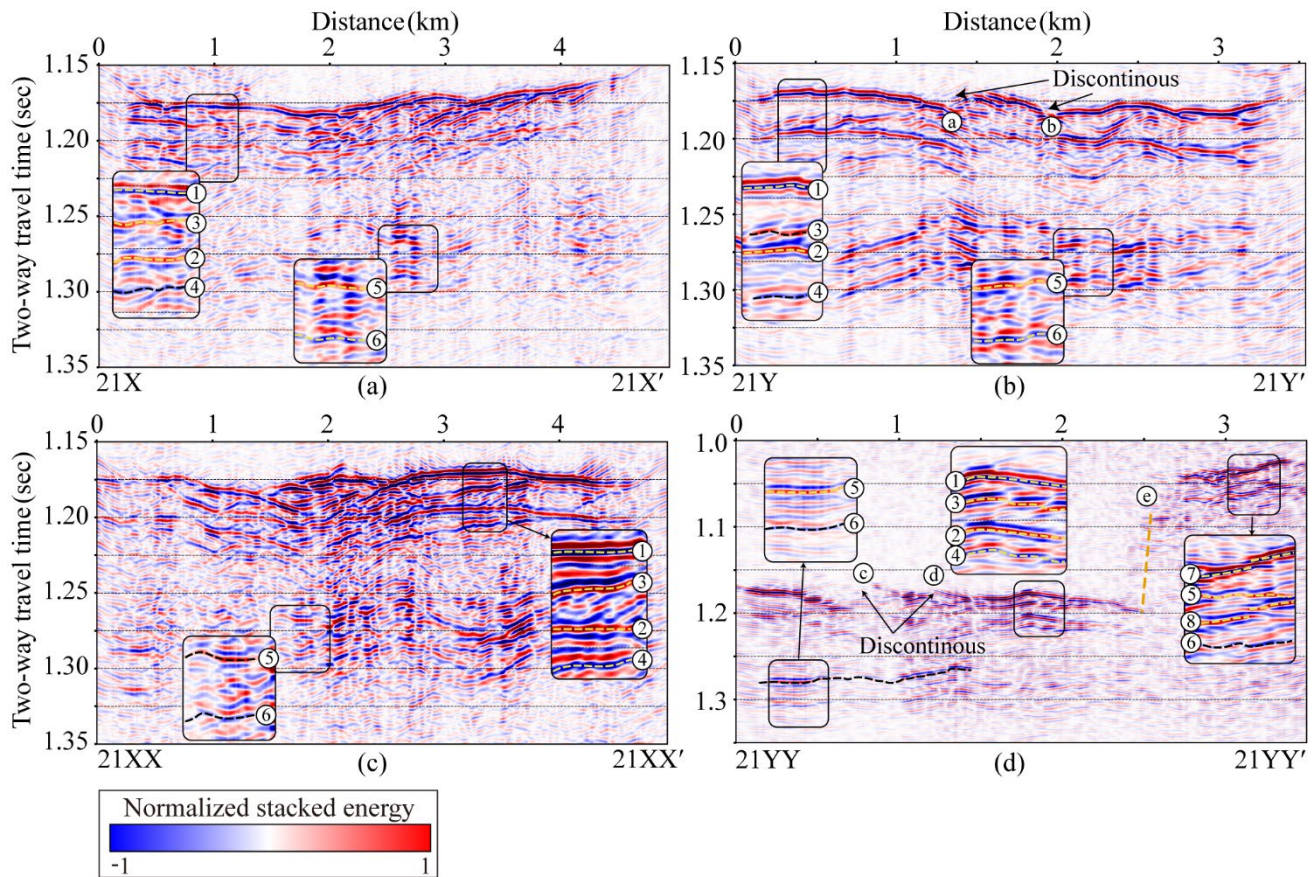
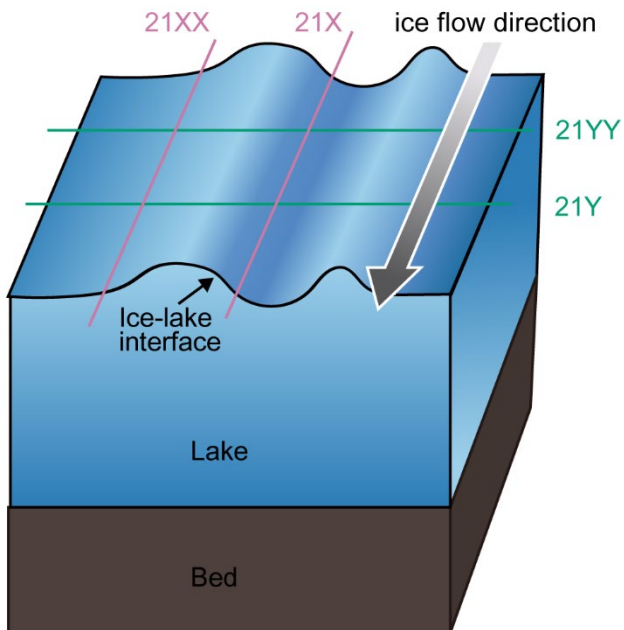


Figure 6: PSTM seismic sections for lines (a) 21X, (b) 21Y, (c) 21XX, and (d) 21YY prior to ghost removal. Ghost reflections appear 25–30 ms beneath the glacier–lake and lake–bed interfaces due to the 25 m source depth. [See Table 2 for symbols definitions.](#)

In line 21Y (Fig. 6b), similar features are observed. A reverse-polarity reflection, interpreted as the glacier–lake interface (1), is observed within 0.1–3.2 km at TWT 1.17–1.18 s, with its ghost reflection (2), which exhibits normal polarity and appears 25–30 ms later. [Between reflections \(1\) and \(2\), a weak normal polarity reflection \(3\), presumed to represent an interface, is observed in some areas, followed approximately 25 ms later by an opposite polarity ghost reflection \(4\).](#) A normal-polarity reflection within 0.1–3.2 km at a TWT of 1.26–1.27 s is interpreted as the lake–bed interface (3–5), followed by a reverse-polarity ghost signal (4–6). Additionally, discontinuous reflections interpreted as subglacial scour-like features (SLF) are visible at approximately 1.3 km (a–a) and 1.9 km (b–b) along line 21Y at TWT 1.18 s (black arrows in Fig. 6b). These features may be associated with glacial erosion of the underlying substrate.

In line 21XX (Fig. 6c), a reverse-polarity reflection, interpreted as the glacier–lake interface (1), is observed within 0–4.3 km at a TWT of 1.17–1.18 s. This reflection is followed 25–30 ms later by a normal-polarity reflection (2), which is considered the ghost of the primary glacier–lake interface. [Between reflections \(1\) and \(2\), a weak normal polarity reflection](#)

276 (3), presumed to represent an interface, is observed in some areas, followed approximately 25 ms later by an opposite polarity
277 ghost reflection (4)). Further down the section, a normal-polarity reflection (3)(5) within 1.9–4.2 km at a TWT of 1.25–
278 1.28 s is interpreted as the lake-bed interface, followed by its ghost reflection (4)(6) 25–30 ms later.
279 On line 21YY (Fig. 6d), the glacier-lake interface (1) is marked by a strong, flat, reverse-polarity reflection at 0–2.4 km and
280 a TWT of 1.17–1.20 s, followed by its normal-polarity ghost (2) 25–30 ms below. Lake bedA weak normal polarity
281 reflection (3), presumed to represent an interface, is observed between (1) and (2), followed approximately 25 ms later by a
282 opposite polarity ghost reflection (4)). Bed interface reflections (3)(5) are observed within 0.2–2.4 km at TWTS of 1.27–
283 1.29 s, followed by a reverse-polarity ghost (4)(6) 25–30 ms later. Within 2.4–2.55 km and TWTS of 1.08–1.17 s, no coherent
284 reflection is visible due to the steeply dipping bed topography, as indicated by the dashed orange (e) line in Fig. 6d. Within
285 2.55–3.4 km and a TWT of 1.03–1.09 s, a stair-step-shaped-reverse polarity reflection at the glacier bed interface (3)(7),
286 likely originating from a mildly dipping sedimentary surface, is identifiedobserved, followed by its reverse-an opposite polarity
287 ghost (4) reflection (8)). Additionally, although weak, reflection signal (5) and its corresponding ghost (6) are also
288 identified. Additionally, similar to observations on line 21Y, discontinuous reflections interpreted as SLF surfaces appear at
289 0.7 km (c) and 1.2 km (4)(d) along line 21YY at TWT 1.18 s (black arrows in Fig. 6d).
290 The discontinuous reflection signals identified on lines 21Y and 21YY are spatially aligned along the ice flow direction when
291 projected laterally (Fig. 3, dashed blue arrow). This alignment suggests that the observed discontinuities correspond to a
292 subglacial SLF surface formed by glacial motion. The SLF is visible predominantly on lines 21Y and 21YY, which are oriented
293 more perpendicularly to the ice flow direction, thereby enhancing the expression of lateral subglacial variability. In contrast,
294 lines 21X and 21XX are more parallel to the ice flow, resulting in a foreshortened view of the subglacial structures and a
295 relatively flat appearance in the seismic sections (Fig. 7).
296



297

298 **Figure 7: Conceptual diagram illustrating the orientation of seismic survey lines relative to subglacial structures and the ice flow**
 299 **direction, explaining the appearance of structural features in each line.**

300

301 **5 Comparison between field data and synthetic seismograms**

302 ~~The depth estimation~~ In all seismic profiles, the glacier–water interface (①) is characterized by strong, reverse polarity
 303 reflections. Following this, a relatively weaker reflection (③) with limited lateral continuity, which may indicate an
 304 unconsolidated sediment layer, or an unknown interface beyond the scope of current interpretation.

305 Interpreting field seismic data presents inherent challenges due to limited subsurface structures information, high levels of
 306 ambient noise, and signal attenuation. These issues are particularly pronounced at the SLD2 site, where the absence of borehole
 307 data introduces significant uncertainty and potential inaccuracies in depth estimations derived from PSTM sections is subject
 308 to errors arising primarily from inaccuracies or uncertainties in the seismic velocity model. An inaccurate velocity model may
 309 result in erroneous positioning of reflection events, leading. Such limitations may lead to misinterpretations
 310 of stratigraphic horizons boundaries (Herron, 2000; Yilmaz, 2001). Such limitations are typically mitigated through well tie
 311 analysis, wherein seismic horizons are calibrated against borehole data. However, in the case of SLD2, no borehole data are
 312 currently available.

313 We validate the processed field data by performing To address these challenges, this study developed a subsurface structural
 314 model and conducted a comparative analysis with synthetic seismograms to address this constraint. The generated from the
 315 model with observed field data. Focusing on the interpretation of basal reflections beneath the subglacial lake—excluding the

316 glacier–lake interface (1)—two plausible structural models were proposed. Model 1 assumes the absence of a sedimentary
 317 layer, in which reflection (3) is not present, and reflection (5) represents the base of the subglacial lake. In contrast, Model
 318 2 includes a sedimentary layer, where reflection (3) corresponds to the lake–sediment interface and reflection (5) indicates
 319 the sediment–bedrock interface (Figure 8). The synthetic data were generated using a time-domain forward modeling
 320 algorithms approach based on the staggered grid finite difference method in the time domain were used (Graves et al., 1996).
 321 The velocity model for this seismic modeling is used in the simulation was constructed by structural information given by the
 322 seismic migration sections, integrating based on field velocity analysis and previously published values of P wave velocities
 323 for data, and included stratigraphic units representing firn, glacial ice, and subglacial water, sediment, and bedrock. Each layer
 324 was assigned appropriate P-wave velocities and density values. P-wave velocities in firn vary from 1525 to 3800 m s⁻¹ because
 325 density increases with depth (Kirchner and Bentley, 1979; Picotti et al., 2015; Qin et al., 2024). Glacial ice has an average P-
 326 wave velocity of approximately 3800 ± 5 m s⁻¹ at -2 ± 2 °C (Kohnen, 1974), while subglacial water has a velocity of
 327 approximately 1396 ± 2 m s⁻¹ at -1.75 ± 0.25 °C, with a salinity less than 1 PSU (practical salinity units) (Thoma et al., 2010;
 328 Tulaczyk et al., 2014). Additionally, on line 21 YY, the reflection polarity at the ice–bedrock interface appears as normal
 329 polarity, which indicates an increase in the acoustic impedance. In other words, this suggests that the P-wave velocity of the
 330 bedrock is higher than that of the overlying ice. Therefore, the bedrock P-wave velocity was set to 4000 m s⁻¹. Using this
 331 information, a layered P-wave velocity model comprising firn, glacial ice, subglacial lakes, and bedrock was developed (Fig.
 332 8). The P-wave velocities of the sediment and bed were referenced from the Lake Vostok model value (Carcione & Gei, 2003).
 333 Forward modeling was then conducted using the Ricker wavelet, with acquisition parameters matching those used in the field
 334 survey (Table 23). We applied just the migration step in case of the synthetic dataset, as it is free of noise.
 335

336 **Table 23: Parameters of the synthetic model.**

	Synthetic modeling parameters		
	Thickness (m)	Velocity (m/s)	Density (g/cm ³)
Model size	3.5 km (distance) x 3 km (depth)		
Source	Ricker wavelet (zero-phase), 60 Hz		
Receiver	25 m depth, 90-m interval		
Grid spacing	0 m depth, 15-m interval, 96 channel		
Sampling interval	0.5-m		
Layer parameters			
Firn	100	<u>1,525–3,800</u>	<u>1525–3800</u>
Ice	<u>1,887–2,221</u>	<u>3,800</u>	<u>3800</u>
Water (Model 1, 2)	<u>01887–2221</u>	<u>1,396</u>	<u>1396</u>
Sediment (Model 2)	<u>53–82+1.3 / 10</u>	<u>2817</u>	<u>2.128</u>
Bed	<u>723–1,113</u>	<u>5200</u>	<u>3.2±1</u>

338

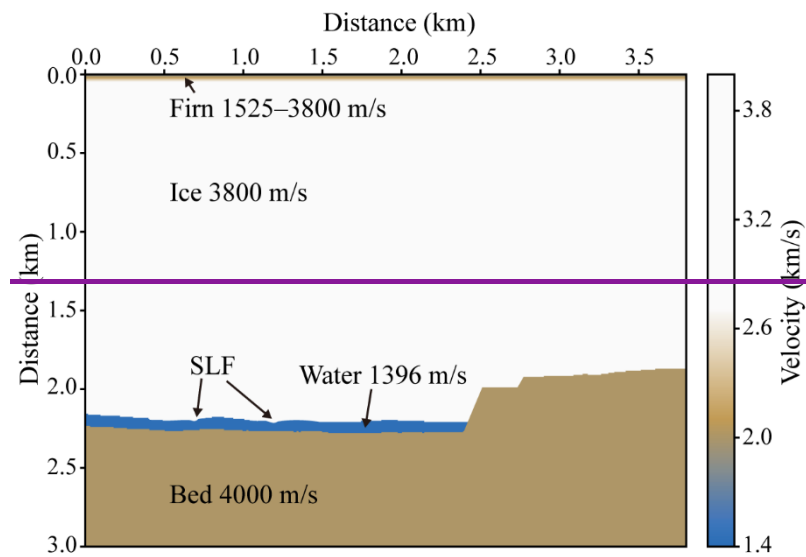
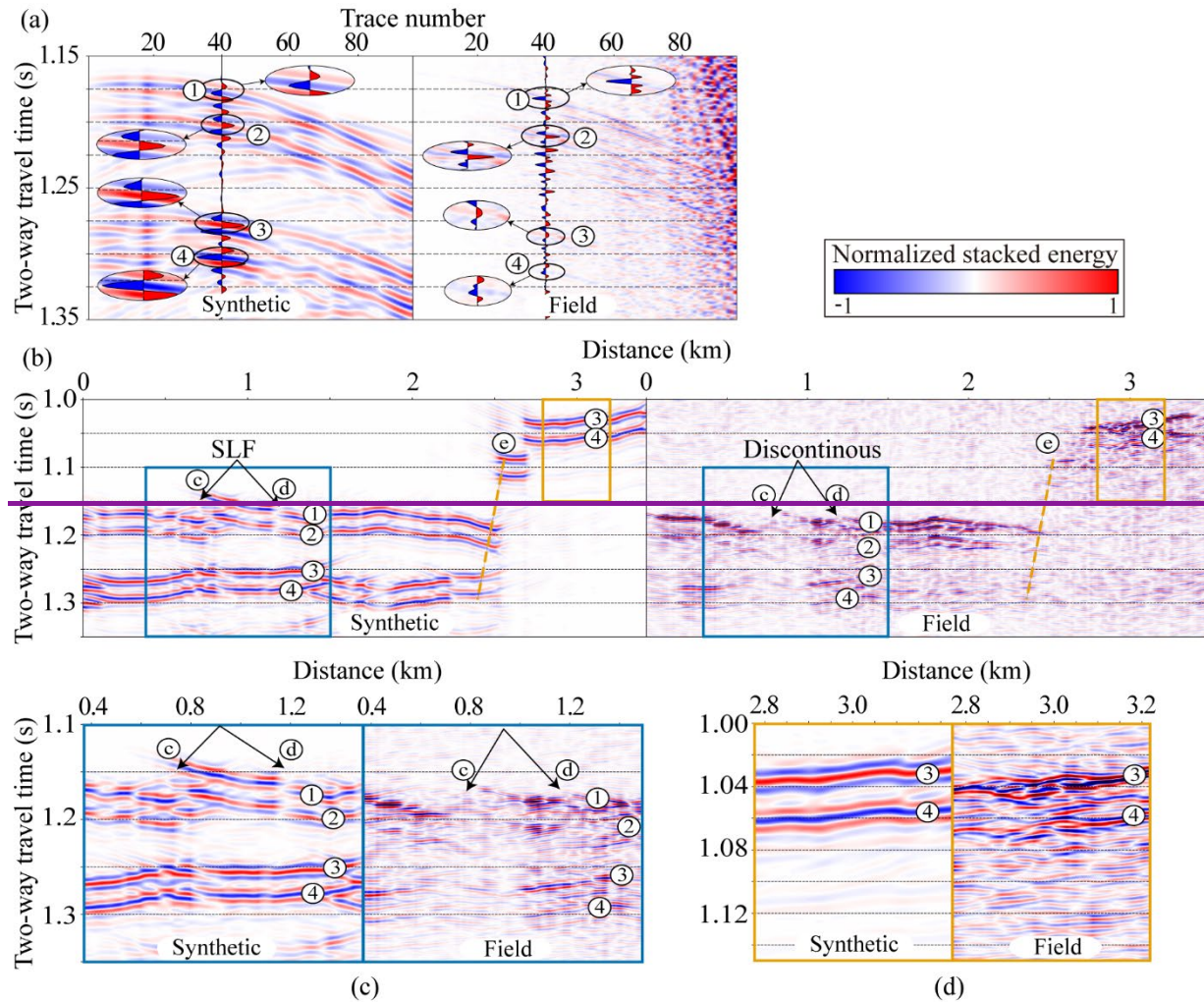


Figure 8: P-wave velocity model used in forward modeling for line 21YY. The upper ~100 m represents firn with velocities ranging from 1525–3800 m s⁻¹ (Kirchner and Bentley, 1979; Picotti et al., 2015; Qin et al., 2024). The ice below this depth has a velocity of 3800 ± 5 m s⁻¹ (Kohnen, 1974), and the subglacial water layer has a velocity of 1396 ± 2 m s⁻¹ (Thoma et al., 2010; Tulaczyk et al., 2014). In Model 2, the velocity of 2817 m s⁻¹ for the sediment layer was taken from the lower sediment layer model of Lake Vostok (Carcione & Gei, 2003).

350 are consistent with previous observations at glacier–lake interfaces (Atre and Bentley, 1993; Brisbourne et al., 2023; Horgan
 351 et al., 2012; King et al., 2004; Peters et al., 2007; Woodward et al., 2010). A secondary reflection with normal polarity appears
 352 approximately 28 ms after the primary event (②) and is interpreted as a surface ghost reflection. This time delay corresponds
 353 to a seismic source depth of approximately 25 m, which is consistent with previous seismic analyses (Brisbourne et al., 2023;
 354 Schlegel et al., 2024). That is, assuming an average P-wave velocity of 1800 m s^{-1} within the top 25 m, the TWT of the ghost
 355 reflection matches the expected delay:

356
$$\text{TWT}_{\text{ghost}} = \frac{2 \times 25 \text{ m}}{1800 \text{ m/s}} \approx 28 \text{ ms.} \quad (1)$$

357



358

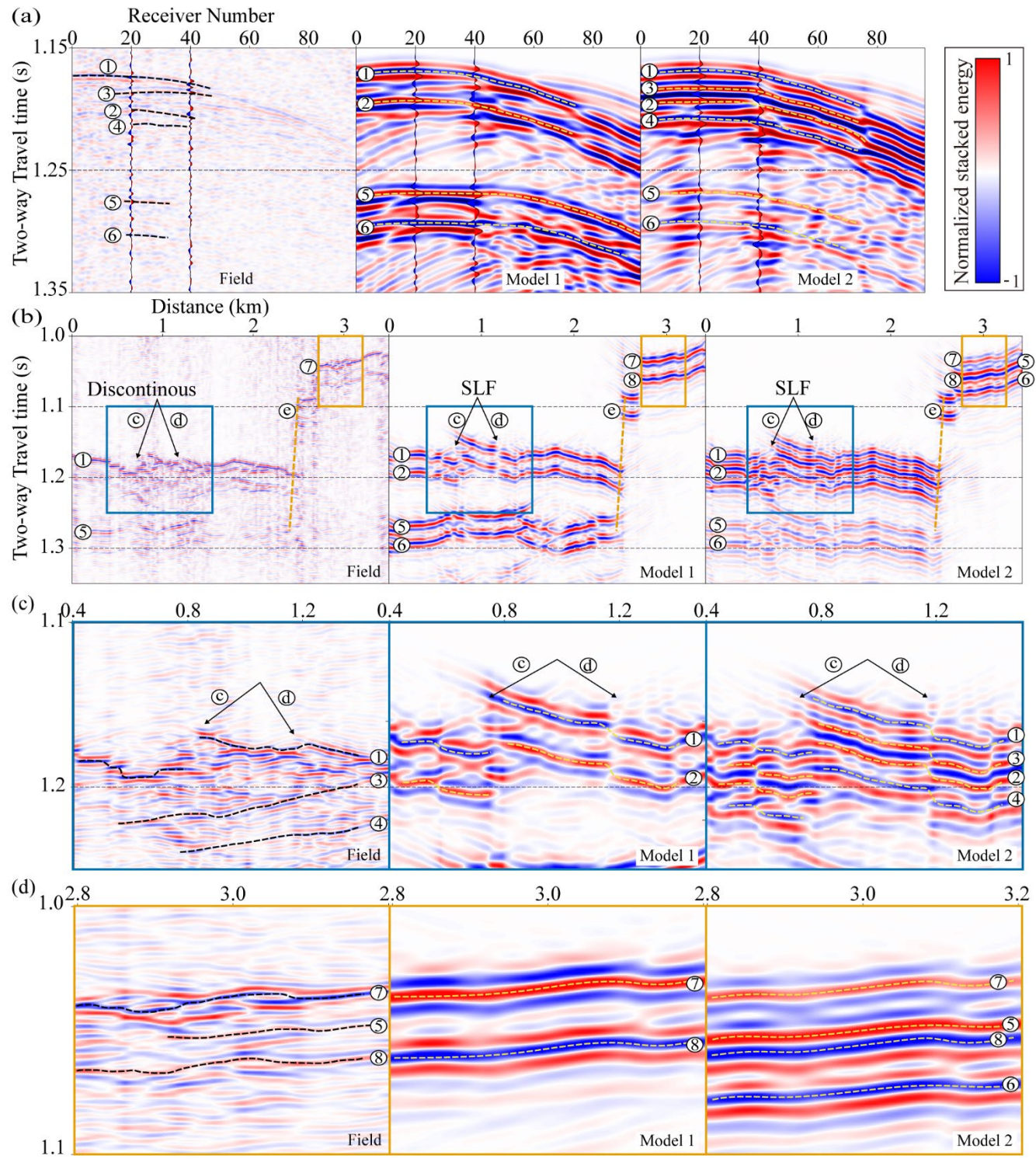
359 **Figure 9: Comparison of synthetic and field seismic data.** (a) Shot gather at the same location for synthetic (left) and 21YY field data
 360 (right). (b) PSTM images comparison between the synthetic model and the 21YY line. (c) Enlarged views of discontinuous
 361 reflections (synthetic, field). (d) Comparison of dipping bed reflections (synthetic, field), showing shadow zones and steep basal topography.

362

363 Furthermore, considering that the acoustic impedance of air is approximately zero ($Z_{air} \approx 0$) and that of ice is Z_{ice} , the
364 reflection coefficient (RC) for an upgoing wave at the air–ice interface can be approximated as follows:

365
$$RC = \frac{Z_{air} - Z_{ice}}{Z_{ice} + Z_{air}} \approx -1. \quad (42)$$

366 This implies that the polarity of the ghost reflection at the surface is reversed relative to the downgoing primary wave (Krail
367 and Shin, 1990; Robinson and Treitel, 2008).



369 **Figure 9: Comparison of field seismic data and synthetic results from Model 1 and 2. (a) Shot gathers at the same location from the**
370 **21YY field data (left) and synthetic models (center: Model 1, right: Model 2). (b) Comparison of PSTM images from the 21YY line**
371 **and the two synthetic models. (c) Enlarged views of discontinuous reflections. (d) Comparison of dipping bed reflections, showing**
372 **shadow zones and steep basal topography.**

373
374 Figure 9b compares the PSTM sections of the synthetic model (left) and the field data from line 21YY (right)and the two
375 synthetic models. Unlike the field data, the synthetic dataset is free from ambient noise and features a precise source-receiver
376 geometry, resulting in clearer delineation of subsurface reflections and facilitating structural interpretation. The In the PSTM
377 sections of both the synthetic models (Model 1 and Model 2) and the field PSTM sections exhibit four principal data, three
378 primary reflection events ((1) (4), (5), (7)) and their corresponding source-generated ghost reflections ((2), (6), (8)) are
379 observed at identical TWTs: similar two-way travel times. Reflections (1) and (4) are characterized by reverse polarity, whereas
380 (2) and (3) display normal polarity, which is ((2), (5), and (6)) also exhibit consistent polarity across both datasets.
381 Discontinuous reflections observed in the synthetic and field datasets. Additionally, the lateral discontinuities in reflections
382 generated by the SLF structure implemented in the velocity model are resemble those observed in the field data. The
383 orange dashed line (e) delineates the shape of the bedrock forming the margin of the subglacial lake, interpreted as indicative
384 of a subglacial SLF surface to dip at approximately 52°.

385 Figure 9c provides a magnified comparison of regions synthetic and field, with a focus on discontinuous features. Although
386 the discontinuous reflections and associated low impedance at 0.7 km and 1.2 km (TWT = 1.18 s) in the field data are
387 challenging to resolve, the SLF surface beneath the glacier is imaged in the synthetic section.

388 Figure 9c presents an enlarged comparison between the field and synthetic PSTM sections, focusing on the region of lateral
389 reflection discontinuities. In the field data, discontinuous reflections and associated low reflectivity observed at approximately
390 0.7 km and 1.2 km (TWT = 1.18 s) complicate interpretation. To simulate this feature, the velocity model incorporates a
391 concave structure at the beneath the glacier, representing the SLF. The resulting reflection patterns in the synthetic section
392 closely resemble those observed in the field data. In the field data, the reflection from the water-sediment interface ((3)) is
393 weak and poorly defined, resulting in significant interpretational uncertainty. This is attributed in part to the diffusive interface
394 of the unconsolidated upper sediment, which weakens reflection strength. Moreover, the short temporal separation between
395 reflection ((3)) and the preceding ghost reflection ((2)) results in significant waveform interference, often producing a single,
396 high-amplitude composite signal. Overlap between reflections ((2)) and ((3)) leads to destructive interference, further
397 complicating the identification of the interface. In some areas, the ghost reflection ((4)) is unaffected by such interference,
398 allowing for an indirect estimation of the ((3)) interface using ghost travel-time differences. However, due to the difficulty in
399 clearly resolving this interface throughout the dataset, Model 2 was constructed using a uniform geometry derived from the
400 average time interval between reflections ((1)) and ((3)), corresponding to a water depth of 10 m and a sediment thickness of 120
401 m. As a result, the arrival time and waveform characteristics of reflection ((3)) in the synthetic data exhibit slight discrepancies
402 when compared to those observed in the field data.

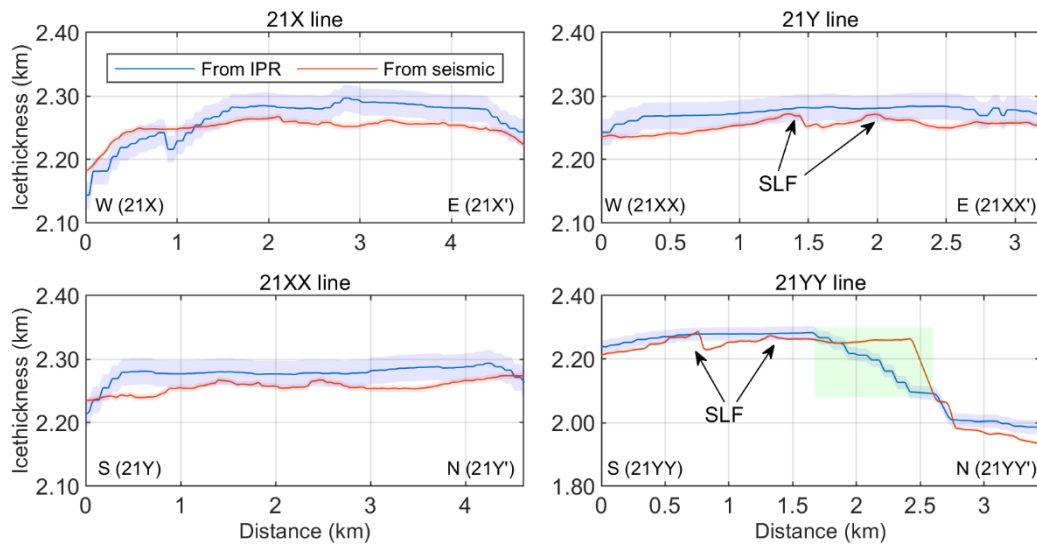
403 Figure 9d presents a magnified comparison of regions synthetic and field to examine reflections from a dipping bed. Within
404 2.4–2.55 km and TWTs of 1.08–1.17 s, reflections are temporally dispersed, resulting in a shadow zone where coherent signals
405 are absent. ~~From 0.2–2.4 km, a reversed-A noteworthy feature is the polarity reflection (1) is observed, whereas from 2.55–~~
406 ~~3.4 km, a normal polarity reflection (3) is present. The latter is interpreted reversal of reflections (7) and (8) between the field~~
407 ~~and synthetic datasets. In the velocity models, the (7) interface is defined as either the glacier bed interface. The dashed line~~
408 ~~traces the steeply dipping bed geometry, delineating the lake margin, with an estimated dip angle of approximately 52°. The~~
409 ~~resulting shadow zone is likely caused by the lateral scattering of bedrock interface in Model 1 or the glacier–sediment interface~~
410 ~~in Model 2. In Model 1, the bedrock has significantly higher acoustic impedance than the overlying ice, due to its greater~~
411 ~~density and seismic energy along the steep slope. The comparison of synthetic PSTM sections confirms that the velocity model~~
412 ~~used for velocity, resulting in a high amplitude reflection with normal polarity. Conversely, the sediment layer in Model 2 is~~
413 ~~assigned a lower seismic imaging appropriately represents the structures of velocity but higher density relative to glacial and~~
414 ~~ice, yielding a slightly higher impedance and thus a reflection of lower amplitude. However, the field data show that reflection~~
415 ~~(7) exhibits reversed polarity, suggesting the presence of subglacial lakesediments with lower acoustic impedance than~~
416 ~~assumed in the models. This discrepancy may be explained by the presence of a dilatant till beneath the glacier, which can~~
417 ~~produce reverse polarity reflections depending on its physical properties. Booth et al. (2012) demonstrated that the seismic~~
418 ~~response of such tills is highly sensitive to variations in P-wave velocity, density, and thickness. In particular, their study~~
419 ~~showed that when the till forms a thin layer, reverse polarity reflections may occur. While the existence of such glacial~~
420 ~~sediments presents a plausible interpretation for the study area, the absence of reliable constraints on their seismic properties~~
421 ~~precluded their incorporation into the velocity models used in this study.~~

422 To further validate the interpretation, ice thickness estimates from the seismic data were compared with those derived from
423 airborne IPR surveys (Ju et al., 2025) along four seismic lines (Fig. 10) (Ju et al., 2025). Given the lack of spatial coincidence
424 between seismic and IPR profiles, kriging-based two-dimensional interpolation (Isaaks and Srivastava, 1989) was applied to
425 the IPR dataset to estimate the ice thickness at seismic line locations. The uncertainties associated with the IPR and seismic
426 datasets are ± 20.98 m and ± 5.27 m, respectively, resulting in a combined uncertainty of ± 24.05 m. The root mean square error
427 (RMSE) between the two datasets is calculated as ± 29.4 m, exceeding this expected uncertainty range. This discrepancy is
428 attributed primarily to smoothing effects introduced by interpolation in the IPR data, particularly between 1.7 and 2.6 km along
429 line 21YY, within the light green shaded area in Fig. 10, where seismic data reveal a significantly steeper basal slope. When
430 this localized region is excluded, the RMSE is reduced to ± 24.8 m, approximating the combined uncertainty. Thus, apart from
431 localized artifacts, the seismic and IPR datasets exhibit strong agreement. This consistency supports the mutual reliability of
432 both methods and validates their integrated application for subglacial lake characterization. Despite localized differences, the
433 overall ice thickness estimates from both datasets are in strong agreement, and this cross-validation reinforces the robustness
434 of the seismic interpretation and affirms the consistency between the two geophysical approaches.

435 As additional supporting evidence for this interpretation, a steeply dipping (approximately 52°) bedrock boundary interface
436 observed along the 21YY line is consistently identified in both the seismic PSTM profile (Figure 9d) and the IPR-derived ice

437 thickness graph (Figure 10), indicating a similar topographic transition in both datasets. This boundaryinterface is interpreted
438 as a structural margin delineating the lateral extent of SLD2 and likely functions as a hydrological barrier. The structural
439 congruence observed in both seismic and radar data underscores the effectiveness of integrating these datasets to delineate the
440 boundaries of subglacial lakes, particularly in regions characterized by complex basal topography.

441



442

443 **Figure 10: A comparison of ice thickness estimates derived from seismic and kriging-interpolated IPR data (Ju et al., 2025)** along
444 the four seismic survey lines reveals high overall consistency between the two datasets, despite localized discrepancies. The light
445 green shaded region in the 21YY line represents areas where interpolation contributes to the divergence between the two
446 measurement approaches. The light blue envelope represents the uncertainty bounds associated with the IPR-derived estimates,
447 while the light red envelope indicates uncertainty bounds for the seismic-derived estimates.

448

449 6 Conclusion

450 Since 2016, the Korea Polar Research Institute (KOPRI) has conducted a series of geophysical investigations to study SLD2
451 (Subglacial Lake Cheongsuk) beneath David Glacier, beginning with airborne IPR surveys. In 2021, a seismic survey was
452 carried out to characterize the internal structure and water column of SLD2. The field seismic data revealed a strong, laterally
453 continuous reflections with reverse polarity reflection at the glacier–lake interface, whereas normal polarity reflections were
454 observed at. In contrast, the glacier bed and basal reflections beneath the lake bed interfaces are less well-defined, suggesting
455 the presence of subglacial sediments. This ambiguity gives rise to two alternative interpretive scenarios based on the presence
456 or absence of a sedimentary layer.

457 A velocity model was constructed on the basis of seismic interpretation, and synthetic seismic data were generated through
458 wave propagation modeling. A comparison between synthetic and field PSTM sections demonstrated strong agreement in the
459 timing and polarity of major reflection events at the glacier–lake and lake–bed interfaces, confirming the validity of the velocity

460 model. This model estimated the ice thickness and lake water column height to be 2250–2300 m and 53–82 m, respectively.
461 These thickness estimates are in close agreement with independent IPR measurements acquired in 2018 (Ju et al., 2025), further
462 supporting the reliability of the seismic interpretation.

463 In lines 21Y and 21YY, discontinuous reflections were observed near the glacier base. The discontinuous signals are
464 interpreted as SLF surfaces formed by basal erosion. Structural alignment across multiple survey lines reveals that these
465 features are oriented in the direction of ice flow, supporting the interpretation of glacial erosion processes at the bed.

466 Given this interpretational ambiguity regarding the sediment layer, two velocity models were constructed: Model 1, which
467 assumes the absence of sediment, and Model 2, which includes a sediment layer beneath the lake. Synthetic seismology was
468 generated using wave propagation modeling based on these models. Sediment thickness in Model 2 was uniformly assigned
469 using the average time difference calculated from selected areas of the dataset. Comparisons between the synthetic and field
470 PSTM sections show consistent TWT times and polarities for key reflection events at the glacier–lake interface, the lake–
471 bedrock interface in Model 1, and the sediment–bedrock interface in Model 2. Nevertheless, synthetic data generated by
472 modeling a velocity model that simplifies a complex geological structure has limitations in thoroughly explaining the entire
473 waveform of the complex field data. For example, subglacial sediments are generally expected to produce normal polarity
474 reflections due to acoustic impedance contrasts with overlying water. However, in field data, the polarity and clarity of the
475 water–sediment interface vary with the degree of sediment consolidation. In particular, the reverse polarity reflection observed
476 at the ice–sediment interface in the 21YY profile suggests the potential presence of dilatant till.

477 This study demonstrates the utility of seismic surveying for analyzing structural characteristics of
478 subglacial lake environments. The that are not identified with conventional radar. Furthermore, the integrated analysis of
479 seismic and synthetic data provides a quantitative constraints on the geometry–structural model of the SLD2-A geometry
480 beneath David Glacier. This study offers These results provide critical insights for future logistical planning, including
481 potential subglacial drilling operations. This study identifies the clean hot-water drilling. In particular, we identify an area
482 within a 1 km radius of S 75.422°, W 155.441° as a suitable candidate site for clean hot water drilling, given, based on its
483 wide broad spatial extent, minimum estimated water depth exceeding approximately 5010 m, and absence of contamination
484 from surface field camps. The site is therefore considered highly appropriate for future exploration of active subglacial lakes.
485 Furthermore, we plan to conduct follow-up studies incorporating advanced processing techniques such as deghosting,
486 amplitude variation with offset (AVO) analysis, and the development of a refined velocity model that accounts for detailed
487 firn-layer properties. These technical advancements are expected to enhance the resolution and precision of seismic imaging
488 and contribute to a deeper understanding of the subglacial environment.

489 Data availability

490 The ICESat-2 data used in this study are available from the National Snow and Ice Data Center (NSIDC). The seismic data
491 and ICESat-2 laser altimetry data used in this study are also available from the Korea Polar Data Center (KPDC) upon request

492 at <https://dx.doi.org/doi:10.22663/KOPRI-KPDC-00001177>. The maps related to Antarctica were created using the
493 Quantarctica dataset version 3.2 (Matsuoka et al., 2018).

494 **Author contributions**

495 HJ: Writing—original draft, investigation, methodology, conceptualization. SGK: Writing—original draft, methodology,
496 conceptualization, supervision. YC: Writing – original draft, data processing, modeling. SP: Data processing methodology.
497 MJL: Writing – original draft. HK: Hot-water drilling. KK: Investigation. YK: Investigation. JIL: Project administration,
498 Funding acquisition.

499 **Competing interests**

500 The authors declare that they have no known competing financial interests or personal relationships that could have appeared
501 to influence the work reported in this paper.

502 **Acknowledgments**

503 We express our sincere gratitude to Sungjun Jeon and the K-route team for their invaluable logistical support. We also extend
504 our appreciation to Do-youn Kwon, Jamin Park, Sanghyeok Seo, and Byeongguk Moon for their dedicated assistance in
505 seismic surveys. We name Subglacial Lake D2 Subglacial Lake Cheongsuk (SLC). The name Cheongsuk has a significant
506 meaning, as it is the pen name of Dr. Yeadong Kim, the founder of the KOPRI and former president of the Scientific Committee
507 on Antarctic Research (SCAR). Dr. Kim personally led the IPR and seismic surveys of Subglacial Lake Cheongsuk and
508 coauthored this paper.

509

510 **Financial support**

511 This research was supported by KOPRI grants funded by the Ministry of Oceans and Fisheries (KOPRI project Nos. PE25070).
512

513 **References**

514 Atre, S. R. and Bentley, C. R.: Laterally varying basal conditions beneath ice Streams B and C, West Antarctica,
515 *J. Glaciol.*, 39, 507–514, <https://doi.org/10.3189/s0022143000016403>, 1993.

516 Bell, R. E., Studinger, M., Shuman, C. A., Fahnestock, M. A., and Joughin, I.: Large subglacial lakes in East
517 Antarctica at the onset of fast-flowing ice streams, *Nature*, 445, 904–907,
518 <https://doi.org/10.1038/nature05554>, 2007.

519 Bell, R. E., Ferraccioli, F., Creyts, T. T., Braaten, D., Corr, H., Das, I., Damaske, D., Frearson, N., Jordan, T.,
520 Rose, K., Studinger, M., and Wolovick, M.: Widespread persistent thickening of the east antarctic ice sheet
521 by freezing from the base, *Science*, 331, 1592–1595, <https://doi.org/10.1126/science.1200109>, 2011.

522 Bentley, M. J., Hodgson, D. A., Smith, J. A., Cofaigh, C. Ó., Domack, E. W., Larter, R. D., Roberts, S. J.,
523 Brachfeld, S., Leventer, A., Hjort, C., Hillenbrand, C. D., and Evans, J.: Mechanisms of Holocene
524 paleoenvironmental change in the Antarctic Peninsula region, *Holocene*, 19, 51–69,
525 <https://doi.org/10.1177/0959683608096603>, 2009.

526 [Booth, A. D., Clark, R. A., Kulessa, B., Murray, T., Carter, J., Doyle, S., and Hubbard, A.: Thin-layer effects in](#)
527 [glaciological seismic amplitude-versus-angle \(AVA\) analysis: implications for characterising a subglacial till](#)
528 [unit, Russell Glacier, West Greenland, *Cryosphere*, 6, 909–922, https://doi.org/10.5194/tc-6-909-2012, 2012.](#)

529 Brisbourne, A. M., Smith, A. M., Rivera, A., Zamora, R., Napoleoni, F., Uribe, J. A., and Ortega, M.:
530 Bathymetry and bed conditions of Lago Subglacial CECs, West Antarctica, *J. Glaciol.*, 69, 1–10,
531 <https://doi.org/10.1017/jog.2023.38>, 2023.

532 [Carcione, J. M., and Gei, D.: Seismic modelling study of a subglacial lake. *Geophysical Prospecting*, 51\(6\), 501–](#)
533 [515. https://doi.org/10.1046/j.1365-2478.2003.00388.x, 2003.](#)

534 Christianson, K., Jacobel, R. W., Horgan, H. J., Anandakrishnan, S., and Alley, R. B.: Subglacial Lake Whillans
535 — Ice-penetrating radar and GPS observations of a shallow active reservoir beneath a West Antarctic ice
536 stream, *Earth Planet. Sc. Lett.*, 331–332, 237–245, <https://doi.org/10.1016/j.epsl.2012.03.013>, 2012.

537 Christner, B. C., Priscu, J. C., Achberger, A. M., Barbante, C., Carter, S. P., Christianson, K., Michaud, A. B.,
538 Mikucki, J. A., Mitchell, A. C., Skidmore, M. L., Vick-Majors, T. J., Adkins, W. P., Anandakrishnan, S.,
539 Barcheck, G., Beem, L., Behar, A., Beitch, M., Bolsey, R., Branecky, C., Edwards, R., Fisher, A., Fricker, H.,
540 Foley, N., Guthrie, B., Hodson, T., Horgan, H., Jacobel, R., Kelley, S., Mankoff, K. D., McBryan, E.,
541 Powell, R., Purcell, A., Sampson, D., Scherer, R., Sherve, J., Siegfried, M., and Tulaczyk, S.: A microbial
542 ecosystem beneath the West Antarctic ice sheet, *Nature*, 512, 310–313, <https://doi.org/10.1038/nature13667>,
543 2014.

544 Dow, C. F., Hubbard, A., Booth, A. D., Doyle, S. H., Gusmeroli, A., and Kulessa, B.: Seismic evidence of
545 mechanically weak sediments underlying Russell Glacier, West Greenland, *Ann. Glaciol.*, 54, 135–141,
546 <https://doi.org/10.3189/2013aog64a032>, 2013.

547 Engelhardt, H., Humphrey, N., Kamb, B., and Fahnestock, M.: Physical conditions at the base of a fast moving
548 Antarctic ice stream, *Science*, 248, 57–59, <https://doi.org/10.1126/science.248.4951.57>, 1990.

549 Filina, I. Y., Blankenship, D. D., Thoma, M., Lukin, V. V., Masolov, V. N., and Sen, M. K.: New 3D bathymetry
550 and sediment distribution in Lake Vostok: implication for pre-glacial origin and numerical modeling of the

551 internal processes within the lake, *Earth Planet. Sc. Lett.*, 276, 106–114,
552 <https://doi.org/10.1016/j.epsl.2008.09.012>, 2008.

553 Frezzotti, M., Tabacco, I. E., and Zirizzotti, A.: Ice discharge of eastern Dome C drainage area, Antarctica,
554 determined from airborne radar survey and satellite image analysis, *J. Glaciol.*, 46, 253–264,
555 <https://doi.org/10.3189/172756500781832855>, 2000.

556 Graves, R. W.: Simulating seismic wave propagation in 3D elastic media using staggered-grid finite differences,
557 *Bulletin of the seismological society of America*, 86, 1091–1106, <https://doi.org/10.1785/BSSA0860041091>,
558 1996.

559 Herron, D. A.: Pitfalls in seismic interpretation: depth migration artifacts, *The Leading Edge*, 19, 1016–1017,
560 <https://doi.org/10.1190/1.1438756>, 2000.

561 Horgan, H. J., Anandakrishnan, S., Jacobel, R. W., Christianson, K., Alley, R. B., Heeszel, D. S., Picotti, S., and
562 Walter, J. I.: Subglacial Lake Whillans — Seismic observations of a shallow active reservoir beneath a West
563 Antarctic ice stream, *Earth Planet. Sc. Lett.*, 331–332, 201–209, <https://doi.org/10.1016/j.epsl.2012.02.023>,
564 2012.

565 Isaaks, E. H. and Srivastava, R. M.: *An Introduction to Applied Geostatistics*, Oxford University Press, Oxford,
566 1989.

567 Johansen, T. A., Ruud, B. E., Bakke, N. E., Riste, P., Johannessen, E. P., and Henningsen, T.: Seismic profiling
568 on Arctic glaciers, *First Break*, 29, 65–71, <https://doi.org/10.3997/1365-2397.20112st1>, 2011.

569 Ju, H., Choi, Y., and Kang, S.-G.: Seismic Survey for the Subglacial Lake in Antarctica. *Geophysics and*
570 *Geophysical Exploration*, 27, 244–257. <https://doi.org/10.7582/gge.2024.27.4.244>, 2024.

571 Ju, H., Kang, S., Han, H., Beem, L. H., Ng, G., Chan, K., Kim, T., Lee, J., Lee, J., Kim, Y., and Pyun, S.:
572 Airborne and Spaceborne Mapping and Analysis of the Subglacial Lake D2 in David Glacier, Terra Nova
573 Bay, Antarctica, *J. Geophys. Res.: Earth Surf.*, 130, <https://doi.org/10.1029/2024jf008142>, 2025.

574 Kim, T., Han, H., Lee, H., and Ju, H.: Monitoring Subglacial Lake Activity in the David Glacier Region, East
575 Antarctica, Using a DInSAR Displacement Integration Approach. IEEE J. Sel. Top. Appl. Earth Obs.
576 Remote Sens., 18, 22175–22192, <https://doi.org/10.1109/jstars.2025.3601588>, 2025.

577 King, E. C., Woodward, J., and Smith, A. M.: Seismic evidence for a water-filled canal in deforming till beneath
578 Rutford Ice Stream, West Antarctica, *Geophys. Res. Lett.*, 31, L20401,
579 <https://doi.org/10.1029/2004gl020379>, 2004.

580 Kirchner, J. F. and Bentley, C. R.: Seismic short-refraction studies on the Ross Ice Shelf, Antarctica, *J. Glaciol.*,
581 24, 313–319, <https://doi.org/10.3189/s0022143000014830>, 1979.

582 Kohnen, H.: The temperature dependence of seismic waves in ice, *J. Glaciol.*, 13, 144–147,
583 <https://doi.org/10.3189/s0022143000023467>, 1974.

584 Krail, P. M. and Shin, Y.: Deconvolution of a directional marine source, *Geophysics*, 55, 1542–1548,
585 <https://doi.org/10.1190/1.1442805>, 1990.

586 Lindzey, L. E., Beem, L. H., Young, D. A., Quartini, E., Blankenship, D. D., Lee, C.-K., Lee, W. S., Lee, J. I.,
587 and Lee, J.: Aerogeophysical characterization of an active subglacial lake system in the David Glacier
588 catchment, Antarctica, *Cryosphere*, 14, 2217–2233, <https://doi.org/10.5194/tc-14-2217-2020>, 2020.

589 Livingstone, S. J., Li, Y., Rutishauser, A., Sanderson, R. J., Winter, K., Mikucki, J. A., Björnsson, H., Bowling, J.
590 S., Chu, W., Dow, C. F., Fricker, H. A., McMillan, M., Ng, F. S. L., Ross, N., Siegert, M. J., Siegfried, M.,
591 and Sole, A. J.: Subglacial lakes and their changing role in a warming climate, *Nature Reviews Earth &*
592 *Environment*, 3, 106–124, <https://doi.org/10.1038/s43017-021-00246-9>, 2022.

593 Matsuoka, K., Skoglund, A., Roth, G., de Pomereu, J., Griffiths, H., Headland, R., Herried, B., Katsumata, K., Le
594 Brocq, A., Licht, K., Morgan, F., Neff, P., Ritz, C., Scheinert, M., Tamura, T., Van de Putte, A., van den
595 Broeke, M., von Deschwanden, A., Deschamps-Berger, C., ... Melvær, Y.: Quantarctica [Dataset].
596 Norwegian Polar Institute. <https://doi.org/10.21334/NPOLAR.2018.8516E961>, 2018.

597 Oliveira, M. S., Henriques, M. V. C., Leite, F. E. A., Corso, G., and Lucena, L. S.: Seismic denoising using
598 curvelet analysis, *Physica A*, 391, 2106–2110, <https://doi.org/10.1016/j.physa.2011.04.009>, 2012.

599 Peters, L. E., Anandakrishnan, S., Alley, R. B., and Smith, A. M.: Extensive storage of basal meltwater in the
600 onset region of a major West Antarctic ice stream, *Geology*, 35, 251–254, <https://doi.org/10.1130/g23222a.1>,
601 2007.

602 Picotti, S., Vuan, A., Carcione, J. M., Horgan, H. J., and Anandakrishnan, S.: Anisotropy and crystalline fabric of
603 Whillans Ice Stream (West Antarctica) inferred from multicomponent seismic data, *J. Geophys. Res. Sol.*
604 *Ea.*, 120, 4237–4262, <https://doi.org/10.1002/2014jb011591>, 2015.

605 Priscu, J. C. and Christner, B. C.: Earth's icy biosphere, in: *Microbial Diversity and Bioprospecting*, edited by:
606 Bull, A. T., ASM Press, Washington, D.C, 130–145, <https://doi.org/10.1128/9781555817770.ch13>, 2003.

607 Qin, L., Qiu, H., Nakata, N., Booth, A., Zhang, Z., Karplus, M., McKeague, J., Clark, R., and Kaip, G.: High-
608 resolution characterization of the firn layer near the West Antarctic ice sheet divide camp with active and
609 passive seismic data, *Geophys. Res. Lett.*, 51, e2024GL108933, <https://doi.org/10.1029/2024gl108933>, 2024.

610 Rignot, E., Mouginot, J., Scheuchl, B., van den Broeke, M., van Wessem, M. J., and Morlighem, M.: Four
611 decades of Antarctic Ice Sheet mass balance from 1979–2017, *P. Natl. Acad. Sci. USA*, 116, 1095–1103,
612 <https://doi.org/10.1073/pnas.1812883116>, 2019.

613 Robinson, E. A. and Treitel, S.: *Digital Imaging and Deconvolution*, Society of Exploration Geophysicists, Tulsa,
614 Okla, 2008.

615 Rose, K. E.: Characteristics of ice flow in Marie Byrd Land, Antarctica, *J. Glaciol.*, 24, 63–75,
616 <https://doi.org/10.3189/s0022143000014659>, 1979.

617 Schlegel, R., Brisbourne, A. M., Smith, A. M., Booth, A. D., Murray, T., King, E. C., and Clark, R. A.:
618 Subglacial bedform and moat initiation beneath Rutford Ice Stream, West Antarctica, *Geomorphology*, 458,
619 109207, <https://doi.org/10.1016/j.geomorph.2024.109207>, 2024.

620 Siegfried, M. R. and Fricker, H. A.: Thirteen years of subglacial lake activity in Antarctica from multi-mission
621 satellite altimetry, *Ann. Glaciol.*, 59, 42–55, <https://doi.org/10.1017/aog.2017.36>, 2018.

622 Siegfried, M. R., Venturelli, R. A., Patterson, M. O., Arnuk, W., Campbell, T. D., Gustafson, C. D., et al. (2023).
623 The life and death of a subglacial lake in West Antarctica. *Geology*, 51(5), 434–438.
624 <https://doi.org/10.1130/g50995.1>

625 Smith, A. M., Woodward, J., Ross, N., Bentley, M. J., Hodgson, D. A., Siegert, M. J., and King, E. C.: Evidence
626 for the long-term sedimentary environment in an Antarctic subglacial lake, *Earth Planet. Sc. Lett.*, 504, 139–
627 151, <https://doi.org/10.1016/j.epsl.2018.10.011>, 2018.

628 Smith, B. E., Fricker, H. A., Joughin, I. R., and Tulaczyk, S.: An inventory of active subglacial lakes in
629 Antarctica detected by ICESat (2003–2008), *J. Glaciol.*, 55, 573–595,
630 <https://doi.org/10.3189/002214309789470879>, 2009.

631 Smith, B. E., Fricker, H. A., Gardner, A. S., Medley, B., Nilsson, J., Paolo, F. S., Holschuh, N., Adusumilli, S.,
632 Brunt, K., Csatho, B., Harbeck, K., Markus, T., Neumann, T., Siegfried, M. R., and Zwally, H. J.: Pervasive
633 ice sheet mass loss reflects competing ocean and atmosphere processes, *Science*, 368, 1239–1242,
634 <https://doi.org/10.1126/science.aaz5845>, 2020.

635 Stearns, L. A., Smith, B. E., and Hamilton, G. S.: Increased flow speed on a large East Antarctic outlet glacier
636 caused by subglacial floods, *Nat. Geosci.*, 1, 827–831, <https://doi.org/10.1038/ngeo356>, 2008.

637 Thoma, M., Grosfeld, K., Smith, A. M., and Mayer, C.: A comment on the Equation of State and the freezing
638 point equation with respect to subglacial lake modelling, *Earth Planet. Sc. Lett.*, 294, 80–84,
639 <https://doi.org/10.1016/j.epsl.2010.03.005>, 2010.

640 Tulaczyk, S., Mikucki, J. A., Siegfried, M. R., Priscu, J. C., Barchek, C. G., Beem, L. H., Behar, A., Burnett, J.,
641 Christner, B. C., Fisher, A. T., Fricker, H. A., Mankoff, K. D., Powell, R. D., Rack, F., Sampson, D.,
642 Scherer, R. P., and Schwartz, S. Y.: WISSARD at Subglacial Lake Whillans, West Antarctica: scientific
643 operations and initial observations, *Ann. Glaciol.*, 55, 51–58, <https://doi.org/10.3189/2014aog65a009>, 2014.

644 Voigt, D. E., Peters, L. E., and Anandakrishnan, S.: ‘Georods’: the development of a four-element geophone for
645 improved seismic imaging of glaciers and ice sheets, *Ann. Glaciol.*, 54, 142–148,
646 <https://doi.org/10.3189/2013aog64a432>, 2013.

647 Wingham, D. J., Siegert, M. J., Shepherd, A., and Muir, A. S.: Rapid discharge connects Antarctic subglacial
648 lakes, *Nature*, 440, 1033–1036, <https://doi.org/10.1038/nature04660>, 2006.

649 Winsborrow, M. C. M., Clark, C. D., and Stokes, C. R.: What controls the location of ice streams?, *Earth-Sci.
650 Rev.*, 103, 45–59, <https://doi.org/10.1016/j.earscirev.2010.07.003>, 2010.

651 Woodward, J., Smith, A. M., Ross, N., Thoma, M., Corr, H. F. J., King, E. C., King, M. A., Grosfeld, K., Tranter,
652 M., and Siegert, M. J.: Location for direct access to subglacial Lake Ellsworth: an assessment of geophysical
653 data and modeling, *Geophys. Res. Lett.*, 37, L11501, <https://doi.org/10.1029/2010gl042884>, 2010.

654 Wright, A. and Siegert, M.: A fourth inventory of Antarctic subglacial lakes, *Antarct. Sci.*, 24, 659–664,
655 <https://doi.org/10.1017/s095410201200048x>, 2012.

656 Yan, S., Blankenship, D. D., Greenbaum, J. S., Young, D. A., Li, L., Rutishauser, A., Guo, J., Roberts, J. L., van
657 Ommen, T. D., Siegert, M. J., and Sun, B.: A newly discovered subglacial lake in East Antarctica likely
658 hosts a valuable sedimentary record of ice and climate change, *Geology*, 50, 949–953,
659 <https://doi.org/10.1130/g50009.1>, 2022.

660 Yilmaz, Ö.: *Seismic Data Analysis: Processing, Inversion, and Interpretation of Seismic Data*, Society of
661 Exploration Geophysicists, Tulsa, Okla, 2001.

662 Zechmann, J. M., Booth, A. D., Truffer, M., Gusmeroli, A., Amundson, J. M., and Larsen, C. F.: Active seismic
663 studies in valley glacier settings: strategies and limitations, *J. Glaciol.*, 64, 796–810,
664 <https://doi.org/10.1017/jog.2018.69>, 2018.